University of Plymouth

PEARL **https://pearl.plymouth.ac.uk**

Faculty of Science and Engineering School of Engineering, Computing and Mathematics

2023-05

Lagrangian modelling of nonlinear viscous waves generated by moving seabed deformation

Renzi, E

http://hdl.handle.net/10026.1/20206

10.1016/j.euromechflu.2023.01.002
European Journal of Mechanics - B/Fluids
Elsevier BV

All content in PEARL is protected by copyright law. Author manuscripts are made available in accordance with publisher policies. Please cite only the published version using the details provided on the item record or document. In the absence of an open licence (e.g. Creative Commons), permissions for further reuse of content should be sought from the publisher or author.

Manuscript File Click here to view linked References

Lagrangian modelling of nonlinear viscous waves generated by moving seabed deformation

E. Renzi[a,*], S. Michele[b], A.G.L. Borthwick[b], A.C. Raby[b]

[a] *Department of Mathematical Sciences, Loughborough University, Leics LE11 3TU, UK*
[b] *School of Engineering, Computing and Mathematics, University of Plymouth, Drake Circus, Plymouth PL4 8AA, UK*

Abstract

A Lagrangian flow model is used to investigate highly nonlinear, dispersive waves generated by moving seabed deformation (MSD) of an otherwise horizontal seabed. Applications include free surface wave responses to horizontal co-seismic displacements and to novel bed-driven wave making systems used in surfing competitions. This paper considers gravity waves in viscous liquid, without restrictions on wave steepness, dispersion coefficient, and flow regime. Numerical computations are carried out using a Moving Particle Explicit method, which provides a Lagrangian flow description with far fewer particles than existing meshless methods. We show that the MSD speed has different effects in shallow and intermediate water depths. In shallow water, raising the MSD speed to a transcritical value promotes generation of leading solitary waves as expected. In supercritical flow, the highly nonlinear dynamics promotes breaking of the precursor soliton. In intermediate depth, wave dynamics is dominated by nonlinearity and dispersion, which act concurrently to generate a large leading wave that travels faster than predicted by linear theory, followed by a train of dispersive, short, steep waves. These waves break, even at subcritical values of MSD speed. We show that strongly nonlinear viscous dynamics occurs in the presence of a steep seabed deformation. This triggers flow separation, linked to strong amplification of wave steepness. Finally, we show that an os-

---

[*] Corresponding author
Email address: `e.renzi@lboro.ac.uk` (E. Renzi)

Preprint submitted to European Journal of Mechanics B / Fluids *November 17, 2022*

cillating MSD is capable of generating higher harmonics by means of nonlinear wave-wave interactions. The model is validated and verified by comparison to previously published experimental data and approximate analytical solutions.

Keywords: Nonlinear waves, particle methods, computational fluid dynamics, tsunamis.

1. Introduction

This paper investigates the fully nonlinear dynamics of viscous gravity waves generated by moving seabed deformation (MSD) over an otherwise horizontal seabed in shallow and intermediate water depths. Our motivation is as follows. (i) Although the problem has been studied extensively in the framework of weakly nonlinear, long-wave theories [1, 2], investigations considering highly nonlinear, dispersive wave regimes are scarce [3]. (ii) The idealised geometry generates robust benchmark cases for further numerical and experimental analysis because waves are generated by a block moving at a prescribed speed, rather than relying on gravity. Complications are avoided from wave reflection at a sloped bed, sudden deceleration at an abrupt transition between an inclined and horizontal bed, and aquaplaning of the solid block at a smooth transition [4]. (iii) The problem is relevant to several important practical applications. For example, the horizontal component of co-seismic displacements contributes significantly to the wave amplitude of earthquake-generated tsunamis, a subject that has not been fully considered to date [5]. A second example concerns novel wave making systems employed in surfing competitions, where waves are generated in a controlled environment by a translating seabed deformation [6, 7].

Related work on gravity waves generated by MSD in inviscid liquid has a long, distinguished tradition. For example, [8], [9] and [10] studied the generation of weakly nonlinear solitary waves by an MSD translating at speed u in shallow water of constant depth h much smaller than the typical wavelength λ such that $\mu^2 = (2\pi h/\lambda)^2 \ll 1$. The wave amplitude ζ considered by the foregoing was also much smaller than λ, i.e. $\epsilon = \zeta/\lambda \ll 1$. The MSD moved at transcritical Froude number $\mathrm{Fr} = u/\sqrt{gh} = 1 \pm \alpha$, where g is gravity and $\alpha \ll 1$ a small nondimensional parameter. The related problem of weakly nonlinear, non-dispersive waves excited by a running stream over an obstacle has also been thoroughly investigated [1, 11, 12]. Recently, Michele *et al.* [13] developed a weakly nonlinear, dispersive model of MSD-generated waves at low Froude number in intermediate water depth, where $\epsilon \ll 1$ but $\mu^2 = O(1)$. Michele *et al.* showed that nonlinearity sharpens the leading elevation wave propagating ahead of the MSD, whereas dispersion shortens the wavelength of trailing waves with respect to the corresponding behaviour in the shallow-water regime.

In this paper, we remove assumptions about wave steepness ϵ and dispersion coefficient μ, and consider gravity wave propagation in a viscous liquid. Few studies have examined how viscosity determines the onset of vorticity in MSD generated waves, limited to shallow water depth [14]. Investigations in this context are also scarce concerning the onset of breaking [3]. Here we examine the nonlinear viscous dynamics of free-surface flow generated by MSD in shallow and intermediate water depths, for subcritical ($\mathrm{Fr} < 0.8$) and transcritical ($0.8 < \mathrm{Fr} < 1.2$) Froude numbers, using a Lagrangian description of the fluid flow.

The vast majority of existing numerical models applied to MSD are based on an Eulerian approach using free surface tracking or capture methods on fixed or adaptive meshes, a typical example being the volume of fluid (VOF) method. However, Eulerian methods encounter difficulties in capturing the free surface when it undergoes large deformation [15]. Furthermore, mesh methods are affected by numerical diffusion associated with the discretisation of the advection term in the governing Navier-Stokes momentum equations [16], particularly when the flow is driven by moving objects [3, 17]. Another limitation of certain VOF solvers, such as IHFOAM, is that the dynamic mesh used to model the seabed deformation has to be sufficiently smooth, i.e., it cannot have vertical edges [3]. Finally, close to breaking, the water column may lose continuity, in which case the free surface elevation cannot be defined. This can cause certain VOF solvers to have a somewhat arbitrary definition of the free surface [3].

The meshless Lagrangian approach is more robust than Eulerian methods because particles are tracked individually, without any limitation to their movement other than that imparted by physical boundaries. The ability to follow each flow particle allows accurate simulation of large deformations and violent flows. The absence of advection terms in the Lagrangian equations of motion means that such methods are free from numerical diffusion [18]. Furthermore, there are hardly any limitations to modelling non-smooth geometries, and application of boundary conditions is straightforward [17, 18]. The main drawback of meshless Lagrangian models is that they require fine discretisation involving a large number of particles, e.g. $O(10^5 - 10^6)$ for a typical Smoothed Particle Hydrodynamics (SPH) simulation of free-surface flow. Consequently such methods are computationally very expensive, and therefore less popular in the context of modelling MSD-generated waves. For example, in the last few decades, few studies of landslide-generated waves have employed a Lagrangian approach [see 15, 19, 20, 21, 22, and references therein].

In this paper, we develop a Lagrangian Moving Particle Explicit (MPE) method, starting from recent work by Renzi & Dias [23] who devised a higher-order Moving Particle Semi-Implicit (MPS) method to model design waves. Renzi & Dias compared predictions by their MPS model with those of Didier *et al.*'s SPH model and experimental data for breaking waves on a breakwater [24]. The MPS model (with 83,418 particles, 15 hours computational time) was able to predict the behaviour of the free surface better and with far fewer particles than the SPH model (154,735 particles, 80 hours computational time). A drawback of the approach taken by [23] is the use of a semi-implicit numerical scheme for pressure, based on empirical coefficients that require further tuning. In the present paper, we improve the model of Ref. [23] by using an explicit algorithm to solve the pressure field. This enables accurate representation of seabed forcing without requiring empirical pressure coefficients. The MPE model used herein is accelerated using parallelisation and vectorisation algorithms in MATLAB, which enable robust convergence with reduced computational execution times of about 50% compared to MPS. The MPE model permits investigation of large free-surface deformations and the onset of vorticity, which arise in sit-

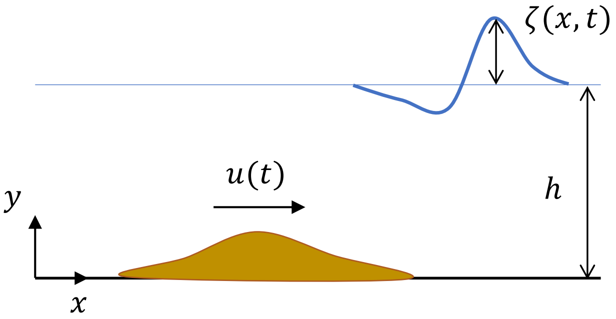

Figure 1: System geometry.

uations where the MSD is irregular or moves at large Froude number. To date, the majority of Lagrangian MSD models have focused on the early stages of an evolving flow, being inefficient for large-scale computations [15, 25, 26]. The enhanced computational performance of the proposed MPE model allows us also to consider long duration wave propagation events.

Section 2 introduces the numerical model and the solution scheme. In Section 3, the model is validated and verified against published experimental data and approximate analytical solutions. Section 4 presents key modelling results, including the effects of viscosity and onset of vorticity for a steep MSD. Conclusions and suggestions for future work follow in Section 5.

2. Numerical model

We present a Numerical Wave Flume (NWF) based on a higher-order MPE method. Referring to Figure 1, we consider a rigid MSD translating at speed $u(t)$ in the horizontal x-direction in water of depth h. The MSD generates gravity waves, whose free surface elevation above still water level is denoted by $\zeta(x,t)$.

2.1. Governing equations

The NWF simulator is based on a Lagrangian description of the fluid flow, whereby the fluid domain is discretised into computational particles, each set an initial distance l_0 from their immediate neighbours. We consider viscous flow of a weakly compressible fluid in two dimensions (x, y), with the y-axis pointing vertically upwards. The horizontal line $y = 0$ denotes the elevation of the seabed (without MSD). The model solves the continuity equation

$$\frac{\mathrm{D}\rho}{\mathrm{D}t} + \rho \nabla \cdot \mathbf{v} = 0, \tag{1}$$

and the Navier-Stokes momentum equation

$$\frac{\mathrm{D}\mathbf{v}}{\mathrm{D}t} = -\frac{1}{\rho}\nabla p + \nu \nabla^2 \mathbf{v} + \mathbf{g}, \tag{2}$$

in which $\mathrm{D}/\mathrm{D}t$ is the Lagrangian derivative with respect to time t, ρ is density, p is pressure, $\mathbf{v} = (u(x, y, t), v(x, y, t))^T$ is the fluid velocity vector, ν is kinematic viscosity and $\mathbf{g} = (0, -g)^T$ is force per unit mass due to the geopotential; $g = 9.81\,\mathrm{ms}^{-2}$ is the acceleration due to gravity.

The governing equations (1)–(2) are solved using a weighted-average scheme, which requires definition of a weight function $w(r, r_e)$. Here we use a third-order spline kernel

$$w(r, r_e) = \left(1 - \frac{r}{r_e}\right)^3 \ \text{ if } r \leq r_e; \quad w(r, r_e) = 0, \ \text{ if } r > r_e, \tag{3}$$

where r_e is an effective radius of interaction and $r = \sqrt{x^2 + y^2}$ is the distance of a particle located at point (x, y) from the origin. Particles lying outside the circle of interaction, of radius r_e, are not considered in the calculation of discretised quantities for the target particle i, see [17, 25]. For a given i-th target particle, the sum of weight functions over neighbouring particles defines its particle number density as

$$n_i = \sum_{j \neq i}^{N_i} w(r_{ji}, r_e), \tag{4}$$

where r_{ji} is the distance between the i-th and j-th particles, and N_i is the total number of particles in the neighbourhood of the target particle i. For simplicity, the upper limit N_i is implicit in the summations from now on.

2.2. Numerical solution

Once the fluid domain is discretised into N particles, the governing equations (1)–(2) are solved by means of a fully explicit algorithm, whereby time is discretised into M intervals $\Delta t = t^{k+1} - t^k$, with t^k denoting the k-th instant, $k = 0, \ldots, M$ and $t^0 = 0$. The discretised governing equations are solved numerically using a predictor-corrector scheme. First, the ith particle velocity $\mathbf{v}_i$ is calculated at an intermediate time step $t^* = t^{k+1/2}$, without considering the pressure gradient:

$$\mathbf{v}_i^* = \mathbf{v}_i^k + \left(\nu \left\langle \nabla^2 \mathbf{v} \right\rangle_i^k + \mathbf{g}\right) \Delta t, \tag{5}$$

where

$$\left\langle \nabla^2 \mathbf{v} \right\rangle_i^k = \frac{4}{\sum_{j \neq l} (r_{jl}^0)^2 \, w\left(r_{jl}^0, r_e\right)} \sum_{j \neq i} \left(\mathbf{v}_j^k - \mathbf{v}_i^k\right) w(r_{ji}, r_e). \tag{6}$$

Then the value is corrected by accounting for the pressure contribution:

$$\mathbf{v}_i^{k+1} = \mathbf{v}_i^* - \frac{1}{\rho} \left\langle \nabla p \right\rangle_i^{k+1} \Delta t. \tag{7}$$

Eqns (5) and (7) give a time-marching algorithm that determines the velocity field at time t^{k+1} from the previous time step, provided the pressure is known for each particle at time t^{k+1}. Hence, an additional equation is required to calculate the pressure field.

The original MPS method considers a Poisson pressure equation (PPE) for incompressible fluid, leading to a sparse linear system for the pressure on each target particle [17]. Usually, such a method is subject to strong numerical instabilities. Suppression of spurious numerical oscillations requires the introduction of corrective terms in the original PPE [23, 18]. For example, the recent MPS method of [23] uses two error-compensating terms in the PPE to improve numerical stability, enabling the model to reproduce design waves of practical interest with a 1% root-mean-square (RMS) error with respect to experimental data. A drawback of [23]'s model is the significant computational time needed by the semi-implicit scheme, and the presence of empirical pressure parameters that require tuning. Here we consider an alternative weakly compressible approach, which is much faster to implement. Allowing for slight compressibility of the fluid, the governing equations (1)-(2) remain valid, in which ρ is the reference ambient density, about which the actual density fluctuates slightly [27, 28]. Hence, (1)-(2) are complemented by the following equation of state used to calculate explicitly the pressure field:

$$p_i^{k+1} = \frac{\rho c^2}{\gamma} \left[\left(\frac{n_i^*}{n_0} \right)^\gamma - 1 \right], \tag{8}$$

where n_0 is the particle number density of an internal particle at $t = 0$, n_i^* is the particle number density of the i-th particle at the intermediate time step, $\gamma = 7$ is the fluid polytropic index, and c is an artificial speed of sound [17, 25, 29, 30, 31]. The equation of state (8) was originally introduced in the context of SPH [30, 32] and applied for the first time to MPS by Shakibaeinia & Jin [29], who defined their method as Weakly-Compressible Moving Particle Semi-Implicit (WC-MPS). Our method extends Shakibaeinia & Jin's formulation by adding further schemes for numerical stabilisation (see Section 2.3) and free-surface stabilisation (Section 2.4). Here we denote our improved method as MPE to highlight the explicit nature of the numerical scheme for pressure.

In order to achieve numerical stability, the artificial speed of sound must be at least 5 times the characteristic speed v_c in the simulation. We therefore set

$$v_c = \max \left\{ \sqrt{gh}, \mathrm{Fr}\sqrt{gh} \right\},$$

with

$$c/v_c \geq 5 \tag{9}$$

ensuring that the maximum density error is of the order of 1% [17]. Others have recommended an even more stringent criterion for numerical convergence, whereby $c/v_c > 10$, e.g. see [32]. We remark that (8) is a stiff equation and is known to introduce unphysical density fluctuations in SPH. In our MPE calculations, we did not observe such fluctuations, so long as condition (9) was satisfied. This is most likely because the MPE method is not based on density per se but on particle number density, which remains more stable throughout the numerical calculations [17]. Furthermore, use of an artificial viscosity term in the

MPE model (see Section 2.3) effectively reduces numerical pressure fluctuations [23].

Once the pressure has been computed, the velocity field is calculated from (7), where the pressure gradient is discretised by means of the following Taylor-expansion based scheme,

$$\langle \nabla p \rangle_i^{k+1} = \mathbf{D}_i^{-1} \cdot \frac{1}{n_0} \sum_{j \neq i} \frac{p_j^{k+1} - \hat{p}_i^{k+1}}{\left(r_{ji}^*\right)^2} \mathbf{r}_{ji}^* \, w\left(r_{ji}^*, r_e\right), \tag{10}$$

where $\mathbf{r}_{ji}^* = (\mathbf{r}_j - \mathbf{r}_i)^*$ is the displacement vector between particles i and j at intermediate time. The vector $\mathbf{r}_{ji}^*$ is readily determined through time integration, such that

$$\mathbf{r}_{ji}^* = \mathbf{r}_{ji} + \left(\mathbf{v}_j^* - \mathbf{v}_i^*\right) \Delta t.$$

In (10), the 2×2 matrix $\mathbf{D}_i$ is given by

$$\mathbf{D}_i = \frac{1}{n_0} \sum_{j \neq i} \frac{\mathbf{r}_{ji}^*}{r_{ji}^*} \otimes \frac{\left(\mathbf{r}_{ji}^*\right)^T}{r_{ji}^*} w\left(r_{ji}^*, r_e\right), \tag{11}$$

[see 17, 23]. If the neighbourhood of the i-th target particle is sparsely populated, $\det(\mathbf{D}_i) \simeq 0$, which would make (10) indeterminate. In such cases, the stabilising matrix $\mathbf{D}_i$ is substituted by the identity matrix.

Choice of the minimum pressure $\hat{p}_i^{k+1}$ in the neighbourhood of particle i makes the numerator in (10) always non-negative; this prevents particle clustering and improves model stability [23]. Note that this only holds for fluid flows of homogeneous density and compressive stress-states, such as those studied here. For fluid flows involving negative pressure and tensile stress state(s), other gradient correction schemes are needed, such as suggested by [33, 34].

With $\mathbf{v}_i^{k+1}$ known, the position of each particle is then updated by simple time integration, as

$$\mathbf{r}_i^{k+1} = \mathbf{r}_i^k + \mathbf{v}_i^{k+1} \Delta t.$$

The time step Δt must satisfy the Courant conditions

$$C_{flow} = v_{max} \Delta t / l_0 < 0.25 \;\text{ and }\; C_{sound} = v_{max} \Delta t / c < 1,$$

and a minimum requirement that $\Delta t < 1 \times 10^{-3}$ s [17, 18].

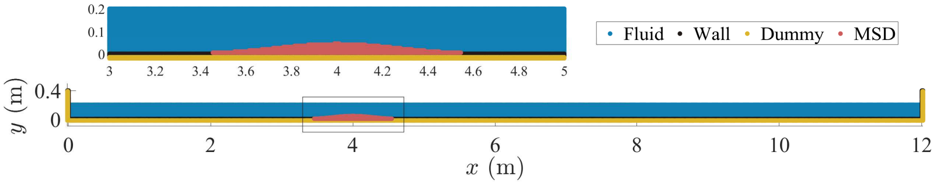

Figure 2: Geometry of the wave flume for a typical numerical experiment. Insert shows detail in the vicinity of the MSD. Legend shows particle types.

2.3. Artificial viscosity

Renzi & Dias [23] recently introduced a novel artificial viscosity term to regularise the numerical calculations, and thus prevent particle explosions and tensile instability. Applying a Moving-Particle Semi-Implicit (MPS) formalism to the earlier SPH formulation of [30], [23] obtained the artificial viscosity term as

$$\left\langle \frac{\mathrm{D}\mathbf{v}}{\mathrm{D}t} \right\rangle_i^k = \frac{\xi c}{n^0}\sum_{j\neq i}\left(\frac{\mathbf{v}_{ji}^k\cdot\mathbf{r}_{ji}^k}{\left(r_{ji}^k\right)^2+0.01r_e^2}\right)\left(\frac{r_e}{r_{ji}^k}\right)^2\frac{\mathbf{r}_{ji}^k}{r_{ji}^k}, \tag{12}$$

where $\mathbf{v}_{ji}^k = \mathbf{v}_j^k - \mathbf{v}_i^k$, $r_{ji}^k = \left|\mathbf{r}_{ji}^k\right|$, and ξ is a non-dimensional tuning parameter that requires calibration. The artificial viscosity term (12) is evaluated at the prediction step (5). The parameter ξ depends on the initial particle distance l_0 and on the flow regime. Noting that the artificial viscosity is different from physical viscosity, calibration of ξ is achieved by minimising the centred root-mean-square error of the time series of the free-surface elevation, with respect to available benchmark data. For free-surface wave applications, ξ is of the order $O(10^{-4} - 10^{-3})$, and variations within this range do not change the dynamics significantly [23].

2.4. Boundary and initial conditions

Figure 2 shows a typical layout of the numerical domain including the MSD and boundaries. Boundary conditions are applied at the free surface of the liquid and at solid boundaries. At each time step, free-surface particles are identified by applying the following criteria concurrently:

$$n_i^k < 0.97 n_0\,; \quad \sum_{j \neq i} \mathbf{r}_{ji} w\left(r_{ji}^k, r_e\right) < 0.88 \sum_{j \neq i} \mathbf{r}_{ji}^0 w\left(r_{ji}^0, r_e\right), \tag{13}$$

as proposed by [23]. Note that a similar criterion, based on a nearly symmetric arrangement of particles (ASA), was implemented in the context of SPH by [35]. Particles that satisfy (13) are assigned a null value of pressure. The free surface elevation ζ is then interpolated numerically using first-order Lagrange polynomials [36].

Solid boundaries (the bed and the two lateral walls of the flume) are modelled using the wall particle method, i.e. they are represented by wall particles that move at the speed of the objects they simulate. Thus, for any particle p belonging to either of the two lateral walls, we apply the non-slip condition $\mathbf{v}_p^k = 0$, at any arbitrary time step k. The bed boundary is represented analytically by the curve $y = f(x,t)$, where $f(x,t)$ is the bed perturbation, starting from rest at $t = 0$ and then moving with speed $\mathbf{u}(t)$ for $t > 0$. Hence any particle q belonging to the MSD must satisfy the initial conditions:

$$(y)_q^0 = f((x)_q^0, 0),\; \mathbf{v}_q^0 = 0.$$

As time elapses, the position of each MSD particle is then updated as

$$(x,y)_q^{k+1} = (x,y)_q^k + \mathbf{u}(t^{k+1})\Delta t.$$

To prevent fluid particles from penetrating solid boundaries, the thickness of wall layers is set at least twice the initial particle distance, and wall particles are assigned pressure in accordance with the equation of state (8). Furthermore, at least two layers of dummy particles are placed behind the wall particles to avoid particle deficiency near the boundaries (see again figure 2).

3. Validation and verification

In this section, we validate and verify the foregoing MPE numerical model against published experimental data and approximate analytical solutions.

3.1. Free-surface elevation for semi-elliptical and Gaussian MSD

First, we consider the seminal experiments of Lee *et al.* [9], performed in an open-topped wave flume 7.5 m long, containing shallow water of mean depth $h = 0.04\,\mathrm{m}$. The waves were generated by a two-dimensional sliding topography of 0.049 m chord and 0.0065 m height at mid-chord. The exact shape of the MSD is not given by [9], and so we assumed a semi-elliptical shape, which is commonly used in experimental investigations on landslide generated tsunamis [3, 19, 20, 21, 37]. We remark that for a smooth sliding body, the exact geometrical shape has only a minor effect on the generated waves [21, 22]. Moreover, this effect becomes negligible in the far field [38].

The MPE model was run with 94,190 particles, time step $\Delta t = 2 \times 10^{-4}\,\mathrm{s}$ and artificial viscosity parameter $\xi = 1 \times 10^{-3}$. Particle number convergence tests were carried out using the statistical method detailed by [23]. Figure 3 shows the evolution of the non-dimensional free-surface elevation, $\eta = \zeta/h$, with non-dimensional time, $T = t\sqrt{g/h}$, for three Froude numbers, $\mathrm{Fr} = 0.82$, 0.89, and 1.01. There is very satisfactory agreement between the numerical and experimental results, except for minor discrepancies in the tails of the wave trains. Table 1 lists the relative error between predicted and measured free surface elevation with respect to still water depth at the largest crest and trough, obtained for each Froude number case considered in figure 3. Note that the relative error invariably remains lower than 10%, corresponding to an absolute error of order $O(10^{-3})\,\mathrm{m}$. This is the same order of magnitude of the initial particle distance $l_0 = 0.002\,\mathrm{m}$ used in the simulations, and is consistent with the use of a first-order Taylor expansion for the gradient scheme (see Section 2.2), where the error is $O(l_0)$. It should be noted that the time series of the slide acceleration is not presented in the paper by [9]. Therefore, in the numerical model we implemented an instantaneous acceleration from initial zero speed, which may further explain the minor differences between the numerical and experimental results. The unevenness of the flume floor ($\pm 0.001\,\mathrm{m}$) and the presence of a small gap ($5 \times 10^{-4}\,\mathrm{m}$) underneath the sliding mass in the experiments are additional factors that could have contributed to the small discrepancies between

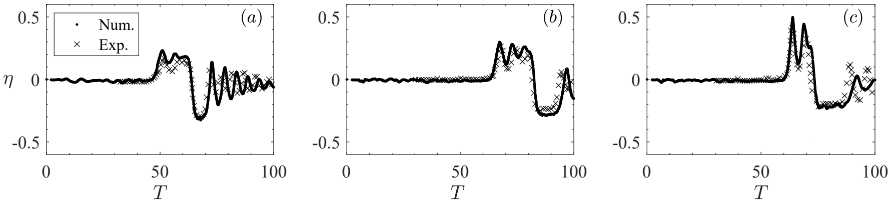

Figure 3: Comparison between non-dimensional free surface time histories obtained using the present numerical model and experimental data from [9]. (*a*) Fr = 0.82, $x/h = 49.3$; (*b*) Fr = 0.89, $x/h = 70$; and (*c*) Fr = 1.01, $x/h = 70$. Note that x is measured downstream of the initial central location of the slide.

Fr	**Crest**	**Trough**
0.82	0.06	0.02
0.09	0.03	0.04
1.01	0.08	0.02

Table 1: Relative error between model predictions and experimental measurements of free surface elevation with respect to water depth h at the largest crest and trough for each case considered in figure 3.

the numerical predictions and published experimental data.

Next, we consider verification against the analytical solution obtained by Michele *et al.* [13]. Figure 4 shows snapshots of non-dimensional free-surface elevation η profiles against non-dimensional horizontal coordinate $X = (x - \bar{x}_c)/h$, obtained using the present MPE numerical model and Michele *et al.*'s analytical solution, $\bar{x}_c$ being the initial position of the MSD centroid. In this case, the seabed perturbation is a translating Gaussian given by

$$f(x,t) = A\mathrm{e}^{-\sigma[x-\bar{x}_c-utH(t)]^2},$$

where u is the horizontal speed of the seabed perturbation, σ is a shape factor, A is the maximum thickness of the perturbation, and $H(t)$ is the Heaviside step function. The parameters are: $\sigma = 7.3\,\mathrm{m}^{-2}$, $A = 0.045\,\mathrm{m}$, $h = 0.2\,\mathrm{m}$. The deformation speed is $u = 1\,\mathrm{m/s}$, corresponding to Fr = 0.71. The MPE model is run with 54,680 particles in a 6 m long numerical flume, the time step is

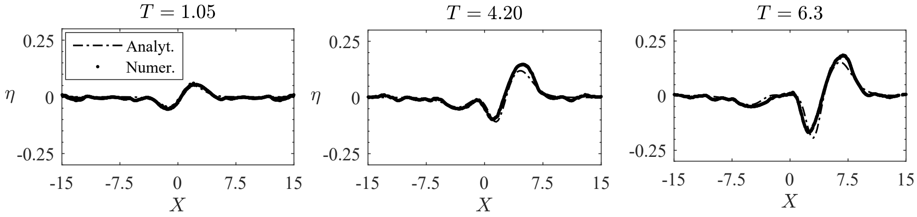

Figure 4: Comparison between the non-dimensional free surface elevation profiles predicted by the present numerical MPE model and the approximate analytical solution proposed by [13] at three non-dimensional time instants.

T	**Crest**	**Trough**
1.05	0.002	0.001
4.20	0.006	0.002
6.3	0.006	0.006

Table 2: Relative error between model predictions and analytical solutions of free surface elevation with respect to water depth h at the largest crest and trough for each case considered in figure 4.

$\Delta t = 5 \times 10^{-4}$ s and the artificial viscosity parameter is $\xi = 2.5 \times 10^{-3}$.

The numerical results in figure 4 provide a close match to the analytical solution, in particular the times of arrival of crests and troughs, and the shape of the wave at different instants. The maximum wave height predicted by the numerical model is slightly higher than that obtained analytically. It should however be noted that the analytical model resolves the wave field up to second order of nonlinearity and so neglects higher-order contributions which can be important near local extrema [13]. Table 2 presents the relative error in predicted and analytical free surface elevation with respect to still water depth at the largest crest and trough, obtained for the cases shown in figure 4. The relative error is below 1%, with absolute error of the same order $O(10^{-3})$ m as that of the initial particle distance $l_0 = 0.005$ m used in the simulations. Appendix A provides details of the convergence of the numerical scheme with initial particle distance. Next, we validate the MPE model using an approximate analytical solution for the case of a rectangular MSD.

3.2. Velocity field close to edge of a rectangular MSD

The velocity field close to the upper edge of a rectangular MSD can be validated against an approximate analytical solution based on a Schwarz-Christoffel conformal mapping [2]. Consider a reference system $(\tilde{x}, \tilde{y})$ moving together with the MSD, so that $\tilde{x} = 0$ on the leading MSD edge and $\tilde{y} = y$. Then the problem becomes that of a step of height d in the bed of a uniform stream. For an observer near the MSD edge, the free surface lies in the far field $\tilde{y}/d \gg 1$, so that an infinite stream depth can be considered in practice.

The fluid domain is mapped to the upper half plane $\zeta = \xi + i\eta$ according to the conformal transformation

$$z = \frac{d}{\pi} \left\{ \sqrt{\zeta^2 - 1} + \cosh^{-1} \zeta \right\},$$

where $z = \tilde{x} + i\tilde{y}$. The complex velocity in the z-plane with respect to the fixed reference system $(\tilde{x}, \tilde{y})$ is

$$\frac{\mathrm{d}w}{\mathrm{d}z} = -U \sqrt{\frac{\zeta - 1}{\zeta + 1}},$$

where U is the flow speed at infinity directed leftwards, and w denotes the complex velocity potential.

Figure 5 shows analytical and MPE predictions of the velocity field close to the edge of a rectangular MSD for the layout investigated later in Section 4. There is very good agreement between the analytical and numerical velocity fields (magnitude and direction) near the vertical edge. However, the potential flow model naturally fails to render the no-slip condition at the boundary between the water and the solid body. Therefore, the results are only comparable in the near field around the edge.

4. Results and discussion

In this section we investigate the influence of Froude number, deformation shape, viscosity, and time-dependent seabed oscillation on the wave field generated by an MSD.

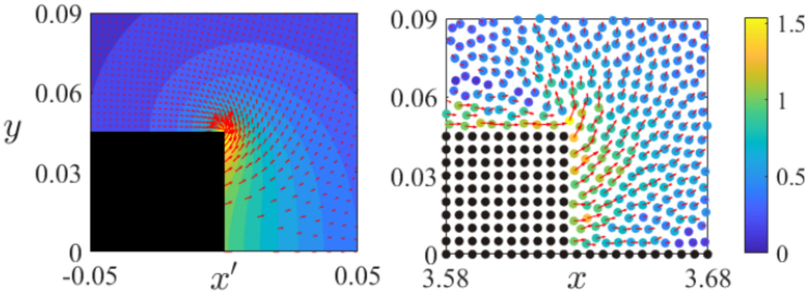

Figure 5: Analytical estimate (left panel, $x' = \tilde{x} + Ut$) and MPE simulation (right panel) of the velocity field (in m/s) near the edge of a rectangular MSD. Parameters are the same as figure 8, coordinates are in metres.

4.1. Influences of Froude number and onset of breaking

Figure 6 shows space-time contour plots of the non-dimensional free-surface elevation in shallow water (figure 6a, b) and intermediate water depth (figure 6c, d) for subcritical (Fr = 0.5) and transcritical (Fr = 0.89) regimes, corresponding to the cases introduced in Section 3. Solid lines show the characteristic curve of a perturbation travelling at linear long-wave speed $c^+ = \sqrt{gh}$, whereas dashed lines represent the MSD trajectory. Dotted lines show the characteristic curve of a perturbation travelling at negative speed $c^- = -\sqrt{gh}$.

In shallow water, an MSD translating at subcritical speed generates a small amplitude, long, leading elevation wave, travelling at near critical speed c^+ (see figure 6a). The crest is followed by a trough travelling just behind the MSD, and then by a train of smaller, shorter waves. There is no noticeable propagation of waves to the left of the MSD. As the Froude number approaches transcritical, the leading free surface elevation wave becomes taller and the depression travelling behind the MSD broadens (see figures 3b and 6b). Further increase in Froude number leads to periodic generation of solitary waves travelling ahead of the disturbance, followed by a depression and a train of cnoidal waves (figure 3c).

In intermediate water depth, the physical picture is different because waves are generated in both directions (figure 6c, d). An MSD travelling at subcritical speed excites a long leading wave that moves at near critical speed c^+ and is

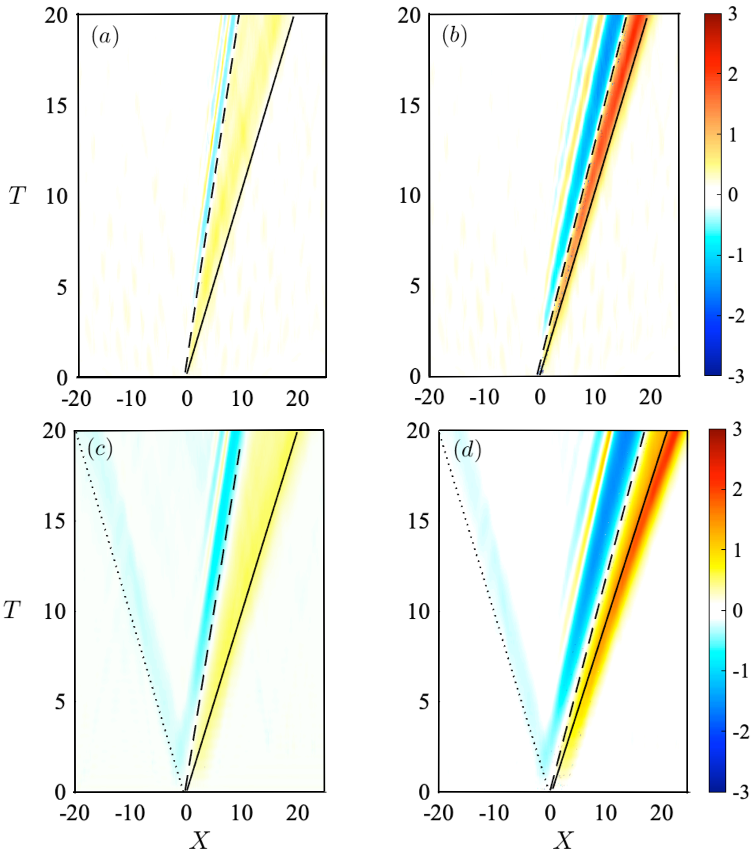

Figure 6: Non-dimensional space-time contour plots of free-surface elevation: (*a*) shallow water depth, same parameters as figure 3, Fr = 0.5; (*b*) shallow water depth, Fr = 0.89; (*c*) intermediate water depth, same parameters as figure 4, Fr = 0.5; and (*d*) intermediate water depth, Fr = 0.89.

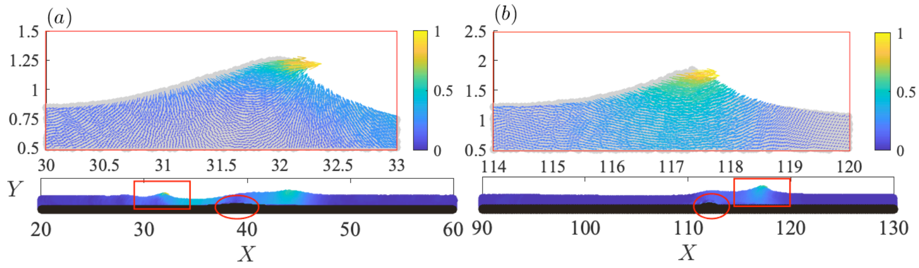

Figure 7: Non-dimensional vector plots of velocity field $\mathbf{v}$ (upper panels) and contour plots of velocity magnitude $|\mathbf{v}|$ (lower panels) at the onset of breaking: (*a*) intermediate water depth, $\mathrm{Fr} = 0.89$, $T = 21.4$; and (*b*) shallow water, $\mathrm{Fr} = 1.12$, $T = 56.4$. Rectangles denote the breaking area, and ellipses highlight the MSD position. The non-dimensional coordinate $X = x/h$, whereas $Y = y/h$.

followed by a depression. The latter travels just behind the MSD and has a larger absolute amplitude (about 0.8) than the leading crest (about 0.4), see figure 6*c*). As time progresses, a tail of weakly nonlinear, fully dispersive waves is generated behind the MSD. Michele *et al.* [13] showed that this trailing wave train can be approximated asymptotically by means of the Airy wave solution. Meanwhile, a shallow trough propagates in the opposite direction to the MSD, at near-critical speed c^-. As the Froude number becomes transcritical, the leading elevation wave again becomes dominant (see figure 6*d*). In intermediate depth, the dynamics is driven by strong nonlinearity and dispersion. As time passes, the leading crest steepens and travels faster than the linear critical speed c^+, leaving an increasingly large gap between the leading crest and the trailing waves. The depression wave persists at MSD speed and broadens as time passes, followed by a tail of nonlinear dispersive waves.

Our numerical experiment shows the emergence of a narrow but steep secondary crest in the trailing wave train (see figure 7*a*). Steepening of the leading crest and the first trailing wave can lead to wave breaking. In intermediate water depth, breaking of the first trailing wave was previously observed experimentally by [3] for $\mathrm{Fr} \geq 0.625$. In shallow water depth, Lee *et al.* [9] reported breaking of the first few trailing waves in shallow water depth at $\mathrm{Fr} \sim 0.8$, when the motion is "sufficiently forced". However, Lee *et al.* also observed breaking of precursor solitary waves at higher Froude number, Fr ~ 1.1. The present numerical model did not predict wave breaking in the shallow-water cases analysed in figure 3. We therefore carried out an additional simulation at Fr $= 1.12$, for which the onset of breaking of the leading soliton occurred (see figure 7*b*). Figure 7 shows that, in both intermediate and shallow water depths, the particle velocity near the crest is horizontal at the point of breaking. Furthermore, the maximum non-dimensional horizontal velocity component is close to unity. Therefore, at the onset of breaking, the horizontal particle velocity component at the crest equals the linear phase speed. This agrees with Stokes' empirical breaking criterion, see [2].

4.2. Effects of viscosity and onset of vorticity

The experiments of [39] showed that a rectangular solid wedge sliding along an incline is able to generate highly nonlinear wave motion along with strong vortices. The vast majority of studies on MSDs consider an inviscid fluid with irrotational motion, and so are inapplicable to vortex dynamics. Recent numerical studies based on a VOF approach considered viscosity [3], but were only applied to smooth MSD.

Here we compare the velocity field generated by a Gaussian-shaped MSD and a rectangular MSD of similar dimensions. The Gaussian bed deformation has the same parameters as in Section 3. The rectangular deformation travels at the same speed as its Gaussian counterpart ($u = 1$m/s) and is 0.65 m long by 0.045 m high, which ensures that the cross-sectional area in the (x, y) plane is the same for both bed deformations.

Figure 8(a, b) shows the spatial variations in magnitude of the velocity field at the onset of motion ($t = 0.2$ s) for the Gaussian and the rectangular MSDs at Fr $= 0.7$, $h = 0.2$ m. The velocity field generated by the Gaussian MSD is smooth and regular, whereas that generated by the rectangular MSD exhibits peaks at the extremities of the rectangular deformation, especially near the trailing edge. Figure 8(c) shows a vector plot of the velocity field around the

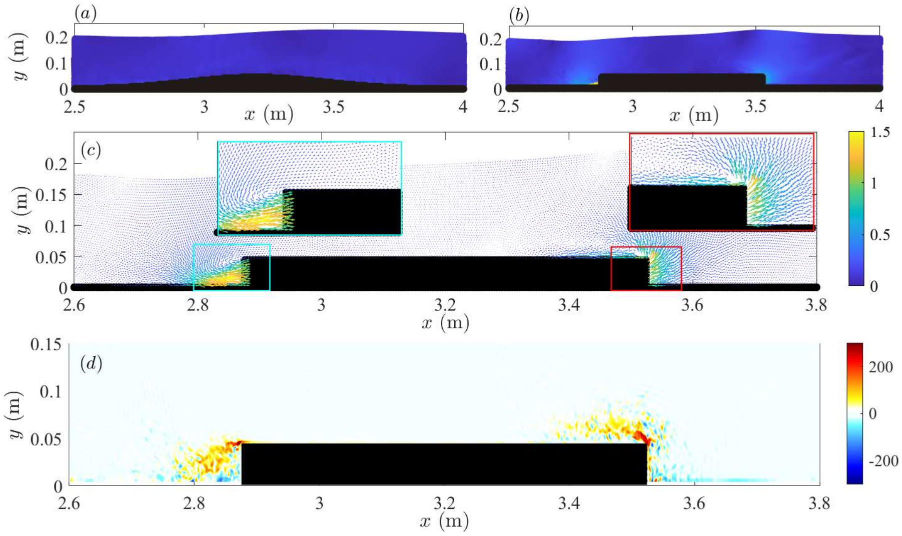

Figure 8: Free-surface elevation and velocity field for: (*a*) Gaussian shaped MSD; and (*b*) rectangular MSD. (*c*) Velocity field for the rectangular MSD. Inserts show detail near the MSD edges. Values are in m/s. (*d*) Vorticity field (in 1/s) for the rectangular MSD. All plots are at $t = 0.2\,\mathrm{s}$, $\mathrm{Fr} = 0.7$. Motion is from left to right.

rectangular MSD. As the deformation travels along the horizontal axis, the vertical edge at the front of the MSD pushes water ahead, producing the leading wave crest. In the lee of the MSD, the fluid moves almost horizontally, driven by a negative dynamic pressure gradient (total pressure p remains positive and so the stress state is in compression), thus generating the trailing trough. This dynamics enhances the steepness of the wave field. Pairs of vortices rotating counterclockwise occur near the front and end edges of the MSD.

Figure 8(d) presents a contour plot of the vorticity field near the rectangular MSD. The Reynolds number is $\mathrm{Re} = h\sqrt{gh}/\nu = 2.79 \times 10^5$. Note that the flow separates at the upper corner of the rectangular cylinder. It is well known that flow past a circular cylinder at similar Reynolds numbers in an unbounded fluid is characterised by vortex shedding behind the cylinder. However, our numerical experiments suggest that the confinement effect due to asymmetric boundaries (free surface on top and seabed at the bottom) suppresses vortex shedding in the present case. Energy that would be otherwise dissipated through vortex shedding instead accumulates, increasing the intensity of the vorticity field to the side of the obstacle. Our results suggest that the presence of strong recirculating areas near the edges of the MSD is linked to the generation of steeper waves (see again figure 8b).

A similar confinement effect has recently been discovered by Zhong *et al.* [40] for flow past a rectangular cylinder close to a free surface. We remark that the laminar viscosity model used in (2) is appropriate to model viscous effects directly only for low-to-moderate Reynolds numbers, e.g. at the onset of motion. When the flow becomes fully turbulent, additional numerical schemes for turbulence modelling are necessary. This remains a key challenge in Lagrangian particle methods [17, 32].

4.3. Analysis of oscillatory motion

In this section, we consider the transient response of initially quiescent liquid to the oscillatory motion of an MSD in an ocean of otherwise constant depth. This provides an idealised representation of horizontal earthquake oscillations, generating benchmark cases for further numerical and experimental analysis. Oscillatory motion of the seabed is also interesting from a theoretical fluid dynamics viewpoint, because resulting wave-wave interactions could promote the generation of higher order wave harmonics.

We consider an MSD moving with variable speed $u(t)$ and fundamental frequency ω. The Keulegan-Carpenter number is $\mathrm{KC} = U\tau/L$, where $\tau = 2\pi/\omega$ is the characteristic period of oscillation and L is the characteristic length scale of the MSD. The KC number could be viewed as the ratio of the amplitude of motion (of the moving bed deformation) to characteristic length of the bed deformation [41]. For oscillatory flow past a bluff cylindrical body (where L is taken to be the cylinder diameter) KC is the ratio of drag to inertia, with [42] reporting that drag becomes significant when $\mathrm{KC} > 15$. Consider a Gaussian-shaped MSD described by

$$f(x) = Ae^{-\sigma(x-\bar{x}_c)^2}. \tag{14}$$

The characteristic dimension L can be taken as the distance between the points where $f(x)$ becomes 1% of its maximum amplitude A, i.e. $L = 3\sqrt{2}/\sqrt{\sigma}$.

Let us investigate the simple case where the Gaussian MSD moves with horizontal speed

$$u(t) = U\sin(\omega t). \tag{15}$$

The MSD is initially centred in the middle of the tank, with centroid located at

$$x_c(t) = \bar{x}_c + \frac{U}{\omega}\left[1 - \cos(\omega t)\right], \tag{16}$$

where $x_c(0) = \bar{x}_c = 6\,\mathrm{m}$. As an example, we consider $U = 0.9\,\mathrm{m/s}$, and $\omega = 1.22\,\mathrm{rad/s}$. All other parameters are the same as in Section 3. The Froude number is $\mathrm{Fr} = U/\sqrt{gh} \sim 0.65$. The Keulegan-Carpenter number is $\mathrm{KC} \sim 3$, therefore inertia effects of an oscillating MSD on the generated wave field are dominant. The contribution of viscous drag for an oscillating MSD will be considered in future work.

In the numerical simulations, the initial particle distance is set at $l_0 = 0.005\,\mathrm{m}$, the flume is 12 m long and the number of particles is 108,680. The

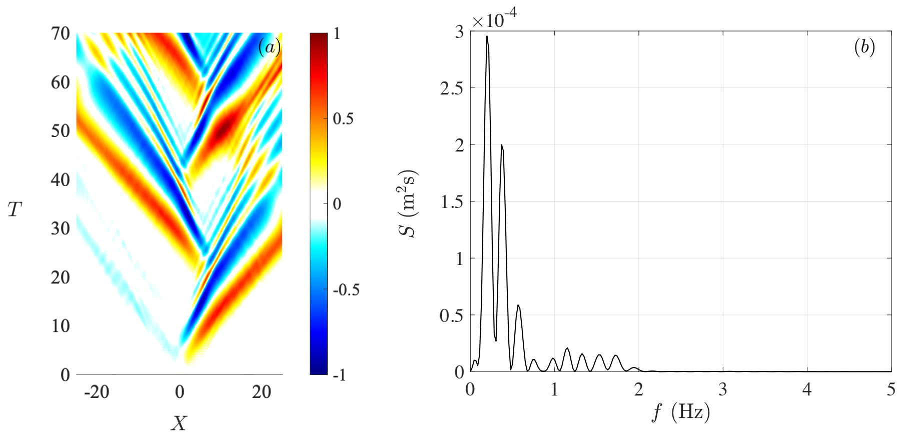

Figure 9: (*a*) Space-time plot of the free surface elevation non-dimensionalised with respect to the MSD height A, for a Gaussian shaped landslide moving with speed $u(t)$ given by (15). (*b*) Energy spectrum of the free surface elevation at $X = 12.5$, corresponding to $x = 8.5\,\mathrm{m}$. The initial position ($X = 0$) of the MSD centroid is $\bar{x}_c = 6\,\mathrm{m}$.

simulation runs over two full oscillation periods, the duration selected to cover the transient regime immediately after the MSD starts to move (of interest in more practical applications). Numerical damping zones of length $5h$ are inserted near the end walls of the flume to minimise reflection. The zones effectively act as dissipative beaches at the ends of the tank. Here the velocity field is prescribed to decrease quadratically [for details see 23].

Figure 9(a) shows that wave trains are generated alternately in both directions. Each wave train features the usual pattern of leading crest, trough and a tail of shorter dispersive waves. Each leading crest travels faster than the trailing waves, and so catches up with the tails of the previous wave train and amplifies the wave height as evident at $(X, T) = (10.5, 50)$. Nonlinear wave-wave interactions give rise to higher harmonic components, as can be seen in the energy spectrum of the free surface elevation depicted in figure 9(b). Most of the energy is carried by the first harmonic component at a forcing frequency $f = \frac{\omega}{2\pi} \sim 0.2$ Hz, with second and third harmonics also generated by nonlinear wave-wave interactions.

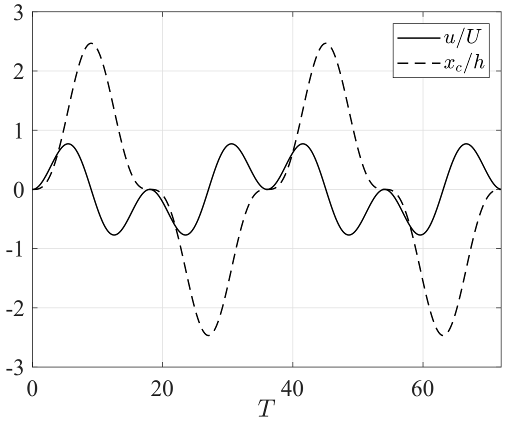

Figure 10: Plots of the centroid speed Eq. (17) and position Eq. (18) in non-dimensional variables.

We remark that the MSD invariably generates a wave train containing multiple frequencies [2, 13]. Dispersion causes individual waves in the wave train to travel at different speeds and have the capacity to interact with waves in preceding or following wave trains, leading to amplification phenomena. The physical picture becomes even more complicated in the nonlinear case, as wave-wave interactions give rise to harmonic generation.

This phenomenon is exemplified by

$$u(t) = U \sin(\omega t) \sin(2\omega t) = \frac{U}{2} \left[\cos(\omega t) - \cos(3\omega t)\right]. \tag{17}$$

This represents a fast oscillation of frequency 2ω modulated by a slower oscillation of sub-multiple frequency ω, which can be also written as the cosine Fourier sum of first and third harmonics. The centroid position is

$$x_c(t) = \bar{x}_c + \frac{U}{2\omega} \left[\sin(\omega t) - \frac{1}{3}\sin(3\omega t)\right], \tag{18}$$

where again $\bar{x}_c = 6\,\mathrm{m}$. The time-series of $u(t)$ and $x_c(t)$ is plotted in figure 10. A space-time plot of the free surface elevation in nondimensional coordinates is shown in figure 11. Note that leading crests and troughs are generated continuously in both directions, as the MSD cyclically reverses its motion, and the wave pattern is more complex than the previous cases.

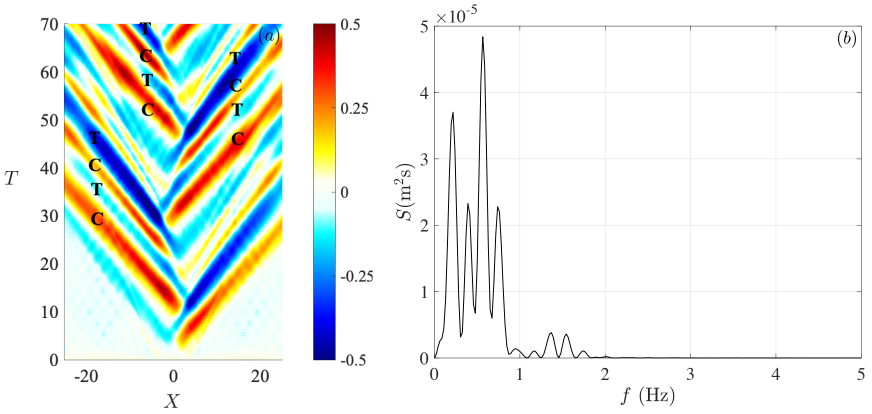

Figure 11: (a) Space-time plot of the free surface elevation non-dimensionalised with respect to the MSD height A, for a Gaussian shaped landslide moving with speed $u(t)$ given by (17). (b) Energy spectrum of the free surface elevation at $X = 12.5$, corresponding to $x = 8.5\,\mathrm{m}$. The initial position ($X = 0$) of the MSD centroid is $x_c = 6\,\mathrm{m}$.

After an initial transient, from $T = 10$ wave trains consisting of large crest-trough groups propagate alternately on either side of the flume (indicated as C-T-C-T in figure 11a). In all these groups, the first crest is more pronounced than the second one, whereas the second trough is deeper than the first one. Figure 11(b) shows the energy spectrum of the free surface elevation at $X = 42.5$, corresponding to $x = 8.5\,\mathrm{m}$. Although most of the energy is concentrated at the forcing frequencies $f \sim 0.2$ Hz and $3f \sim 0.6$ Hz, even harmonics $2f$ and $4f$ are also generated as a result of nonlinear wave-wave interactions. Note also that the 3rd harmonic is the most energetic, suggesting that 3rd order harmonics are generated through nonlinear amplification.

This analysis can be extended to a spectrum of components comprising multiples of the fundamental frequency ω, i.e. by extending the Fourier series (17) to higher harmonics. This would allow modelling more realistic horizontal seabed motions. A method for the separation of the underlying harmonic structure of focused wave groups was proposed by [43] in the context of Stokes-like waves. The method is based on the use of inverse simulations. In an extension of the present work, the moving hump seabed profiles would be replaced by mirrorimage moving trough seabed profiles. The resulting wave elevation time series could be added/ subtracted to give even/odd harmonics, following [43]. Such an analysis has yet to be applied to MSD and would therefore offer an intriguing future research direction.

5. Conclusions

A Lagrangian particle-based model has been used to investigate the highly nonlinear, viscous flow generated by a moving seabed deformation (MSD).

We find that bed deformation speed exerts different influences in shallow and intermediate water depths. In shallow water, transcritical Fr promotes the occurrence of leading solitary waves that travel at near critical speed. Weak nonlinearity is then balanced by weak dispersion, as discussed by [8, 9]. Highly nonlinear dynamics leading to breaking of the precursor soliton occurs in supercritical flow. In intermediate water depth, the dynamics is invariably dominated by nonlinearity and dispersion even at low Froude number. As Fr increases, the leading elevation wave becomes steeper and travels faster than the linear critical speed. Trailing dispersive waves also become increasingly steep, up to the point of breaking.

In both shallow and intermediate water depths, breaking occurs when the horizontal velocity component of a particle at the crest approaches the critical speed. Our results suggest that the first wave to break is the leading solitary wave in shallow water and one of the trailing waves in intermediate water. Furthermore, breaking appears to occur in intermediate water depth at lower values of Froude number than in shallow water. This is a result of the interplay between nonlinearity and full dispersion, which steepens the trailing waves in intermediate water. This result was recently demonstrated analytically by Michele *et al.* [13] and is now confirmed numerically by our model.

Our Lagrangian MPE model allows the simulation of highly nonlinear waves generated by a steep seabed deformation, which was not possible to model using previous Eulerian VOF methods, see for example [3]. Strong nonlinear dynamics occurs in the presence of a rectangular MSD. Pairs of separated vortexes develop near the upper corners of the deformation. Interestingly, the confinement effect of the free surface and seabed prevents vortex shedding, while energy accumulates near the edges of the MSD. Our model suggests that such vortex dynamics is linked to strong amplification of wave steepness even at subcritical Froude numbers.

In this paper, we halted the simulations at the onset of wave breaking. Future investigations are recommended in which the air phase is added to the model so as to reproduce correctly air entrainment in breaking, viscous waves.

Finally, we investigated two cases where the MSD moves with variable speed in an oscillatory motion. The results confirm that dispersive dynamics in intermediate water promotes nonlinear wave-wave interactions which are in turn responsible for the generation of higher harmonic wave components and wave amplification. A theoretical analysis is underway to investigate the underlying harmonic structure of such amplified groups.

Appendix A. Numerical convergence analysis

In this section we examine the numerical convergence of the MPE results. For non-negligible bed deformation and very small kinematic viscosity of water, it is reasonable to expect that the largest contributions to the velocity field in the Navier-Stokes equations (2) are given by the pressure gradient and gravity. Given that the gravity term is calculated exactly, convergence of the MPS model is governed by the numerical approximation of the pressure gradient. As discussed in [23], the error of the Taylor-based expansion (10) for the pressure gradient is of order $O(l_0)$. Hence we expect the numerical results to converge almost linearly with l_0.

For example, consider the case in figure 4, where the initial particle spacing is $l_0 = 0.005\,\mathrm{m}$, corresponding to 54,680 particles. Here we carry out the same simulation, but with $l_0 = 0.01$, corresponding to 15,360 particles.

Figure A.12 shows free surface elevation profiles obtained for the analytical

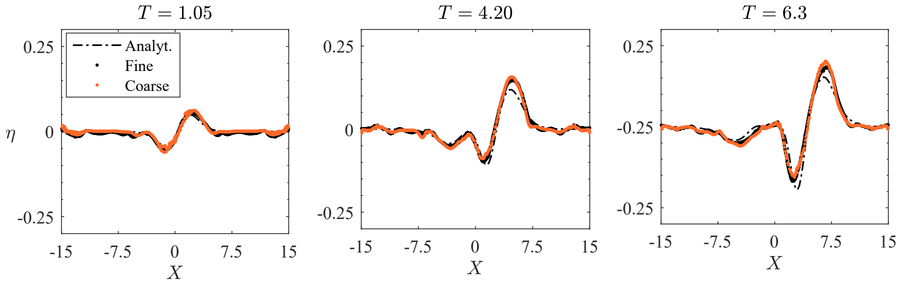

Figure A.12: Comparison between non-dimensional free surface elevation profiles predicted by the present numerical MPE model and the approximate analytical solution proposed by [13] at three non-dimensional time instants.

Coarse:	$l_0/h = 0.05$	**Fine**:	$l_0/h = 0.025$
R	E	R	E
0.9572	0.0149	0.9614	0.0140

Table A.3: Correlation coefficient R and centred root-mean square (RMS) error between present prediction and approximate analytical solution of free surface elevation with respect to depth $h = 0.2m$ for the cases considered in figure A.12.

solution of [13], a coarse-grained simulation using the present model with 15,360 particles (orange line), and a fine-grained simulation with 54,680 particles (black line). Though the plots are very similar, differences appear close to the extremes. Quantitative analysis of the relative error is presented in tables A.3 and A.4.

Table A.3 lists the correlation coefficient R and the centred root-mean-square (RMS) error, calculated according to the method described in [23], for the simulations in figure A.12. Note that in both simulations the RMS error is $E \simeq 1\%$. Increasing the number of particles has the beneficial effect of increasing the correlation coefficient R and decreasing the RMS error E. Table A.4 shows that the maximum relative error in free surface elevation with respect to depth at the wave crest and trough for the fine-grained simulations is 0.006, corresponding to an absolute error of 1.2×10^{-3} m, as already discussed. On the other hand, the maximum relative error for the coarse-grained simulations is 0.01, corresponding to an absolute error of 2×10^{-3} m. Hence halving the initial particle distance

T	**Coarse**:	$l_0/h = 0.05$	**Fine**:	$l_0/h = 0.025$
	Crest	**Trough**	**Crest**	**Trough**
1.05	0.003	0.002	0.002	0.001
4.20	0.008	0.004	0.006	0.002
6.3	0.01	0.008	0.006	0.006

Table A.4: Relative error between model predictions and analytical solutions of free surface elevation with respect to water depth h at the largest crest and trough for each case considered in figure A.12.

approximately halves the maximum relative error. This is in accordance with the theoretical error analysis discussed above and demonstrates that the MPE simulations converge almost linearly with initial particle distance.

References

[1] G. B. Whitham, Linear and nonlinear waves, Wiley, New York, 1974.

[2] C. C. Mei, M. Stiassnie, D. K.-P. Yue, Theory and application of ocean surface waves, World Scientific, Singapore, 2005.

[3] C. J. Whittaker, R. I. Nokes, H.-Y. Lo, P. L.-F. Liu, M. J. Davidson, Physical and numerical modelling of tsunami generation by a moving obstacle at the bottom boundary, Environ. Fluid Mech. 17 (2017) 929–958.

[4] L. P. Sue, R. I. Nokes, M. J. Davidson, Tsunami generation by submarine landslides: comparison of physical and numerical models, Environ. Fluid Mech. 11 (2011) 133–165.

[5] D. Dutykh, D. Mitsotakis, L. Chubarov, Y. Shokin, On the contribution of the horizontal sea-bed displacements into the tsunami generation process, Ocean Model. 56 (2012) 43–56.

[6] J. Dalphin, R. Barros, Optimal Shape of an Underwater Moving Bottom Generating Surface Waves Ruled by a Forced Korteweg-de Vries Equation, J. Optimiz. Theory App. 180 (2019) 574–607.

[7] Wavegarden, www.wavegarden.com. Last accessed: 8/6/2022.

[8] T. Y. Wu, Generation of upstream advancing solitons by moving disturbances, J. Fluid Mech. 184 (1987) 75–99.

[9] S.-J. Lee, G. T. Yates, T. Y. Wu, Experiments and analyses of upstream-advancing solitary waves generated by moving disturbances, J. Fluid Mech. 199 (1989) 569–593.

[10] P. A. Madsen, A. B. Hansen, Transient waves generated by a moving bottom obstacle: a new near-field solution, J. Fluid Mech. 697 (2012) 237–272.

[11] L. Debnath, Nonlinear water waves, Academic Press, Inc., San Diego, CA, 1994.

[12] R. Grimshaw, D.-H. Zhang, K. Chow, Generation of solitary waves by transcritical flow over a step, J. Fluid Mech. 587 (2007) 235–254.

[13] S. Michele, E. Renzi, A. Borthwick, C. Whittaker, A. Raby, Weakly nonlinear theory for dispersive waves generated by moving seabed deformation, J. Fluid Mech. 937 (2022) A8.

[14] D. Zhang, A. Chwang, On solitary waves forced by underwater moving objects, J. Fluid Mech. 389 (1999) 119–135.

[15] S. Yavari-Ramshe, B. Ataie-Ashtiani, Numerical modeling of subaerial and submarine landslide-generated tsunami waves–recent advances and future challenges, Landslides 13 (2016) 1325–1368.

[16] K. Goda, N. Mori, T. Yasuda, A. M. A. Prasetyo, D. Tsujio, Cascading geological hazards and risks of the 2018 sulawesi indonesia earthquake and sensitivity analysis of tsunami inundation simulations, Front. Earth Sci. 7 (2019) 261.

[17] S. Koshizuka, K. Shibata, M. Kondo, T. Matsunaga, Moving Particle Semi-implicit Method, Academic Press, 2018.

[18] H. Gotoh, A. Okayasu, Y. Watanabe, Computational Wave Dynamics, World Scientific, Singapore, 2013.

[19] P. Sammarco, E. Renzi, Landslide tsunamis propagating along a plane beach, J. Fluid Mech. 598 (2008) 107–119.

[20] E. Renzi, P. Sammarco, Landslide tsunamis propagating around a conical island, J. Fluid Mech. 650 (2010) 251–285.

[21] E. Renzi, P. Sammarco, The influence of landslide shape and continental shelf on landslide generated tsunamis along a plane beach, Nat. Hazard Earth Sys. 12 (2012) 1503–1520.

[22] E. Renzi, P. Sammarco, The hydrodynamics of landslide tsunamis: current analytical models and future research directions, Landslides 13 (2016) 1369–1377.

[23] E. Renzi, F. Dias, Application of a moving particle semi-implicit numerical wave flume (MPS-NWF) to model design waves, Coast Eng. 172 (2022) 104066.

[24] E. Didier, D. Neves, R. Martins, M. Neves, Wave interaction with a vertical wall: Sph numerical and experimental modelling., Ocean Eng. 88 (2014) 330–341.

[25] L. Fu, Y.-C. Jin, Investigation of non-deformable and deformable landslides using meshfree method, Ocean Eng. 109 (2015) 192–206.

[26] J. Xie, Y. Tai, Y. Jin, Study of the free surface flow of water–kaolinite mixture by moving particle semi-implicit (mps) method, Int. J. Numer. Anal. Met. 38 (2013) 811–827.

[27] E. Renzi, F. Dias, Hydro-acoustic precursors of gravity waves generated by surface pressure disturbances localised in space and time, J. Fluid Mech. 754 (2014) 250–262.

[28] S. Michele, E. Renzi, Effects of the sound speed vertical profile on the evolution of hydroacoustic waves, J. Fluid Mech. 883 (2019) A28.

[29] A. Shakibaeinia, Y. Jin, A weakly compressible mps method for modeling of open-boundary free-surface flow, Int. J. Numer. Meth. Fl. 61 (2010) 1208–1232.

[30] J. Monaghan, Smoothed Particle Hydrodynamics, Rep. Prog. Phys. 68 (2005) 1703.

[31] M. Jandaghian, A.Shakibaeinia, An enhanced weakly-compressible mps method for free-surface flows, Comp. Method Appl. M. 360 (2020) 112771.

[32] S. Lind, B. Rogers, P. Stansby, Review of smoothed particle hydrodynamics: towards converged lagrangian flow modelling, Proc. R. Soc. A 476 (2020) 20190801.

[33] A. Khayyer, H. Gotoh, Enhancement of stability and accuracy of the moving particle semi-implicit method, J. Comput. Phys. 230 (2011) 3093–3118.

[34] A. Khayyer, H. Gotoh, Enhancement of performance and stability of MPS meshfree particle method for multiphase flows characterized by high density ratios., J. Comput. Phys. 242 (2013) 211–233.

[35] A. Khayyer, H. Gotoh, S. Sao, Enhanced predictions of wave impact pressure by improved incompressible sph methods, Appl. Ocean Res. 31 (2009) 111–131.

[36] H. Aref, S. Balachandar, Computational Fluid Dynamics, Cambridge University Press, 2018.

[37] C. Whittaker, R. I. Nokes, M. J. Davidson, Tsunami forcing by a low froude number landslide, Environ. Fluid Mech. 15 (2015) 1215–1239.

[38] P. H.-Y. Lo, P.-F. Liu, On water waves generated by a bottom obstacle translating at a subcritical speed, J. Fluid Mech. 923 (2021) A26.

[39] P.-F. Liu, T.-R. Wu, F. Raichlen, C. Synolakis, J. Borrero, Runup and rundown generated by three-dimensional sliding masses, J. Fluid Mech. 536 (2005) 107–144.

[40] W. Zhong, L. Deng, Z. Xiao, Flow past a rectangular cylinder close to a free surface, Ocean Eng. 186 (2019) 106118.

[41] Y. Wei, A. Rafiee, A. Henry, F. Dias, Wave interaction with an oscillating wave surge converter, part i: Viscous effects, Ocean Eng. 104 (2015) 185–203.

[42] T. Sarpkaya, M. Isaacson, Mechanics of Wave Forces on Offshore Structures, Van Nostrand Reinhold Company, New York, 1981.

[43] A. Hunt, Extreme waves, overtopping and flooding at sea defences, University of Oxford, 2003.

Click here to access/download;Figure;ancomp.pdf

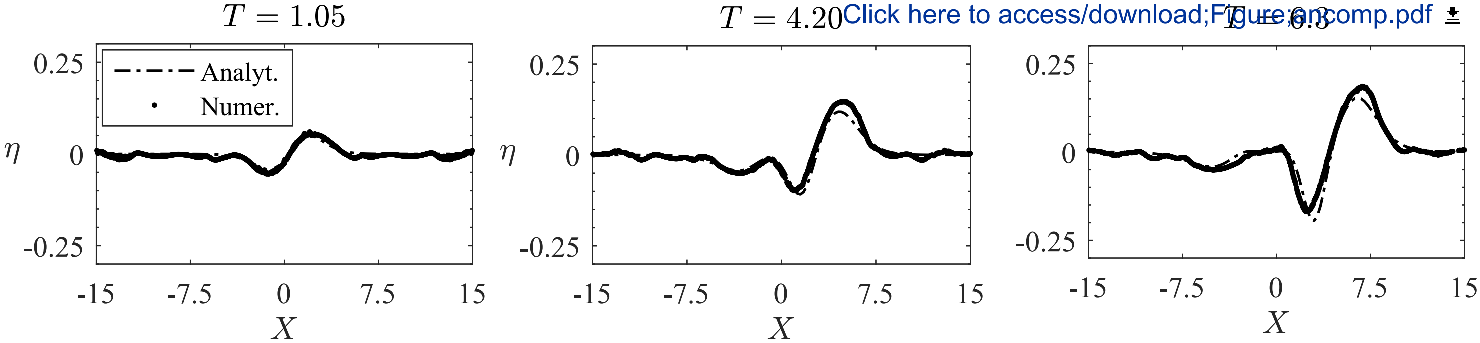

Click here to access/download;Figure;break.pdf

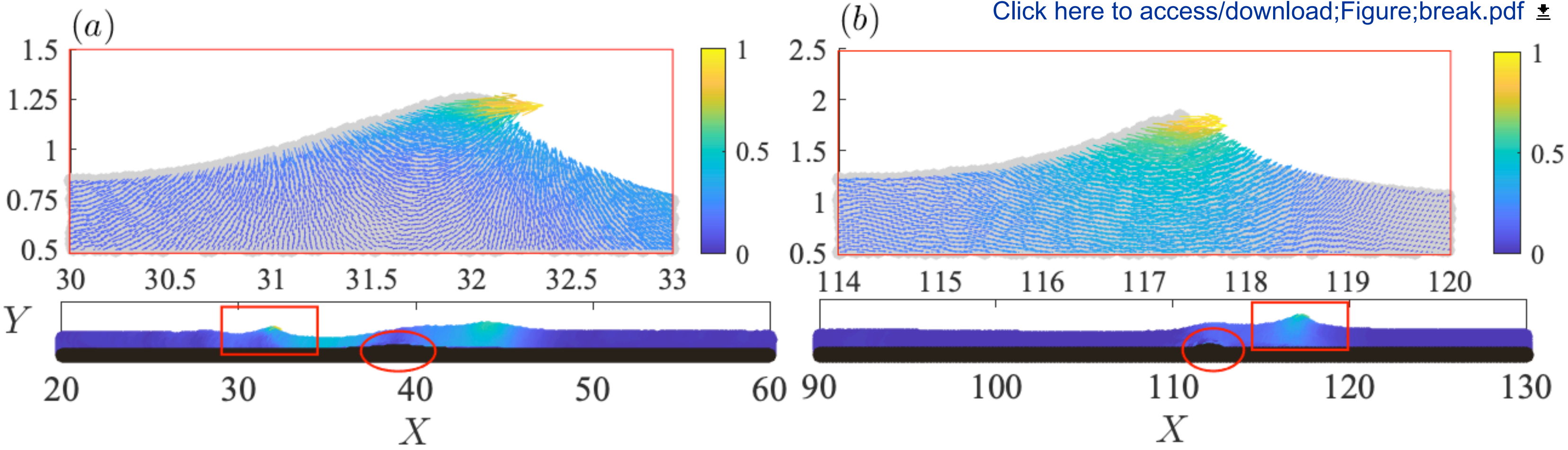

Click here to access/download;Figure;comp_conv.pdf

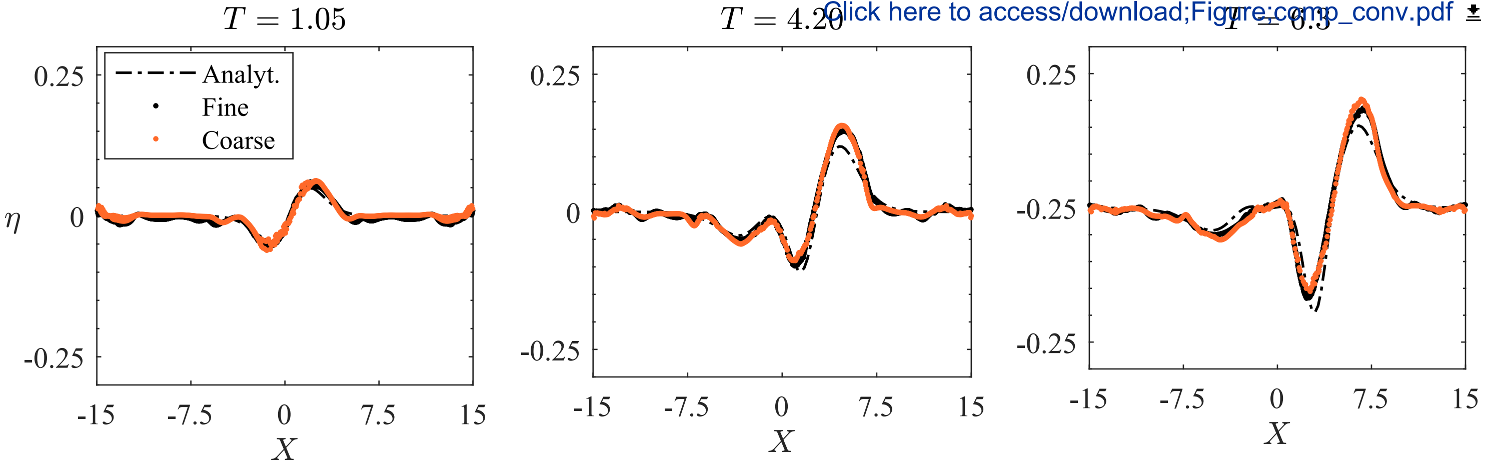

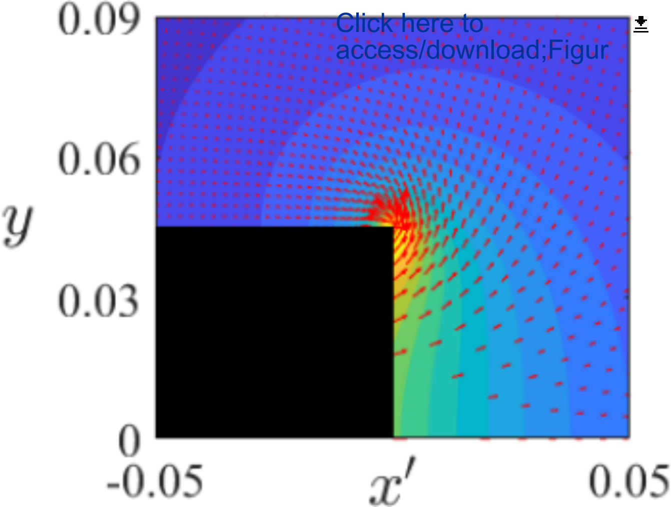
0.09
0.06
0.03
0
y
-0.05
x'
0.05

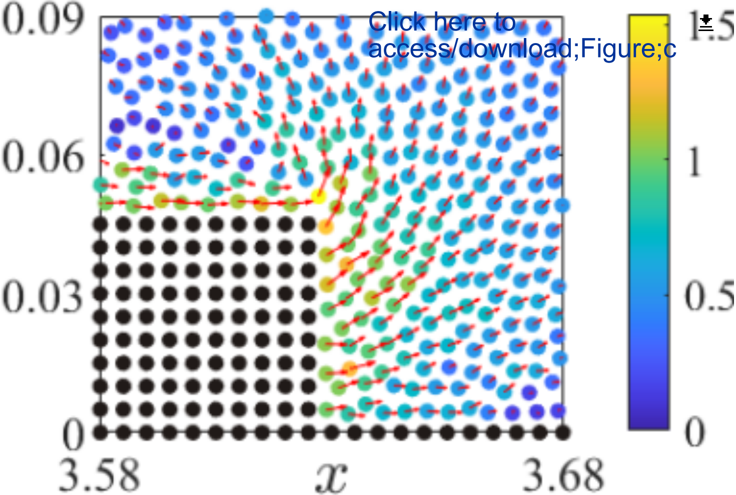
0.09
0.06
0.03
0
3.58
x
3.68
1.5
1
0.5
0

Click here to access/download;Figure;geom.pdf

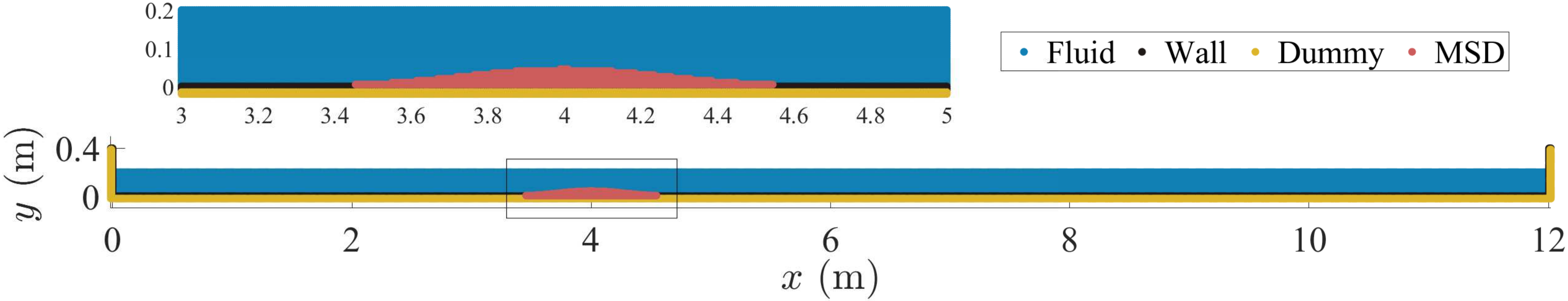

Click here to access/download;Figure;layout.pdf

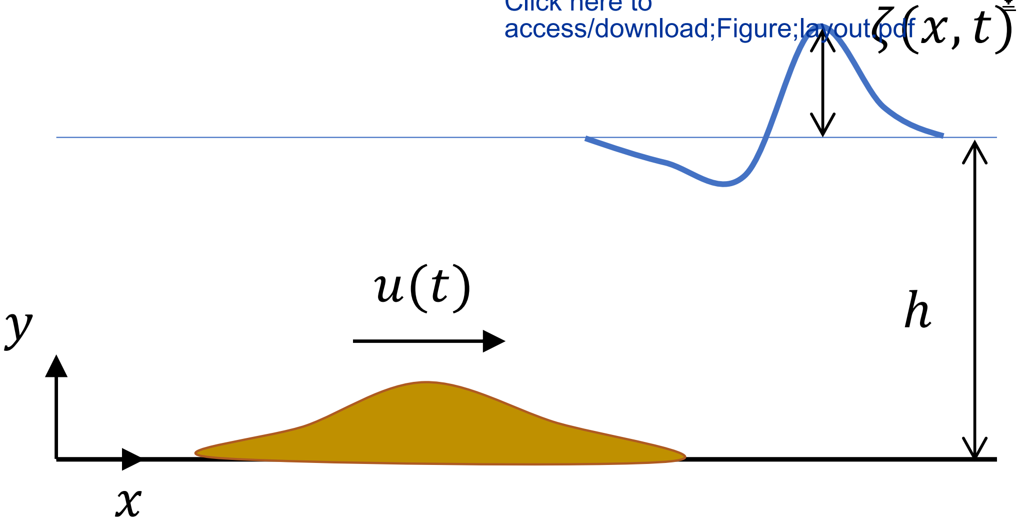
$\zeta(x,t)$
$u(t)$
h
y
x

Click here to access/download;Figure;Leecomp.pdf

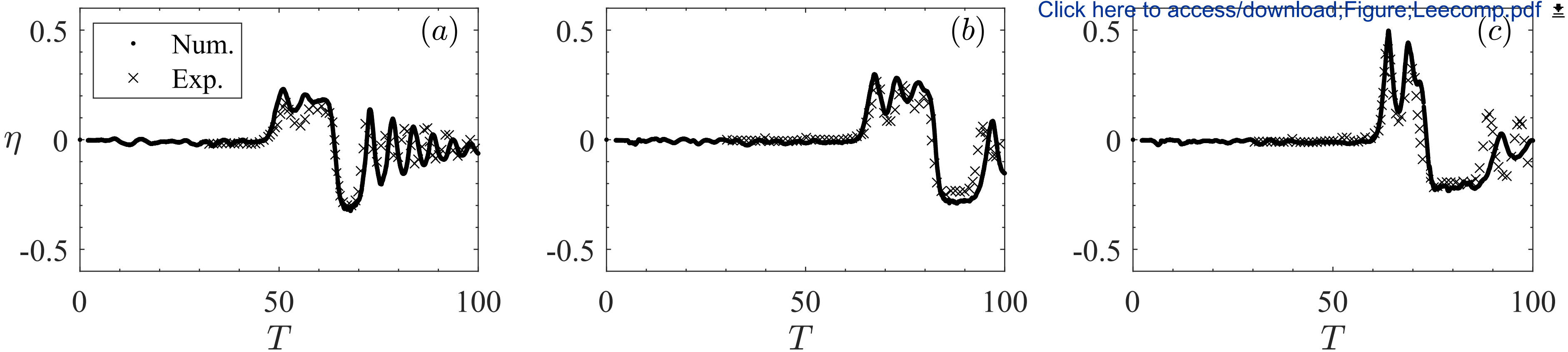

Click here to
access/download;Figure;spacetab.pdf

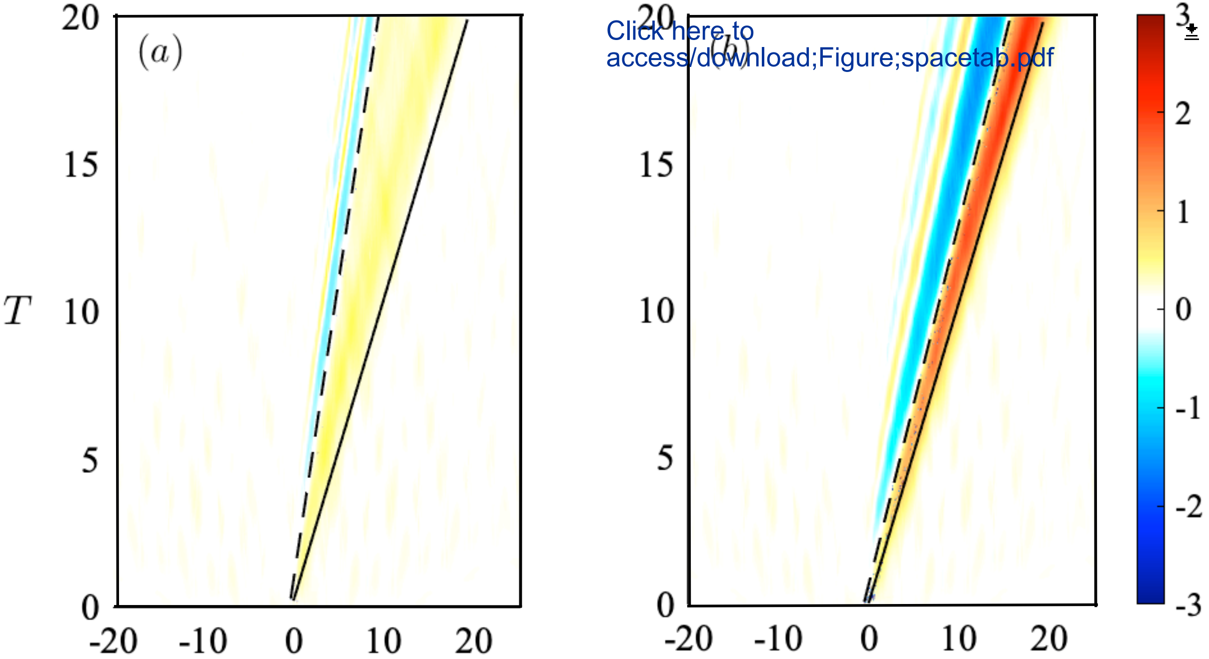

Click here to access/download;Figure;spacetcd.pdf

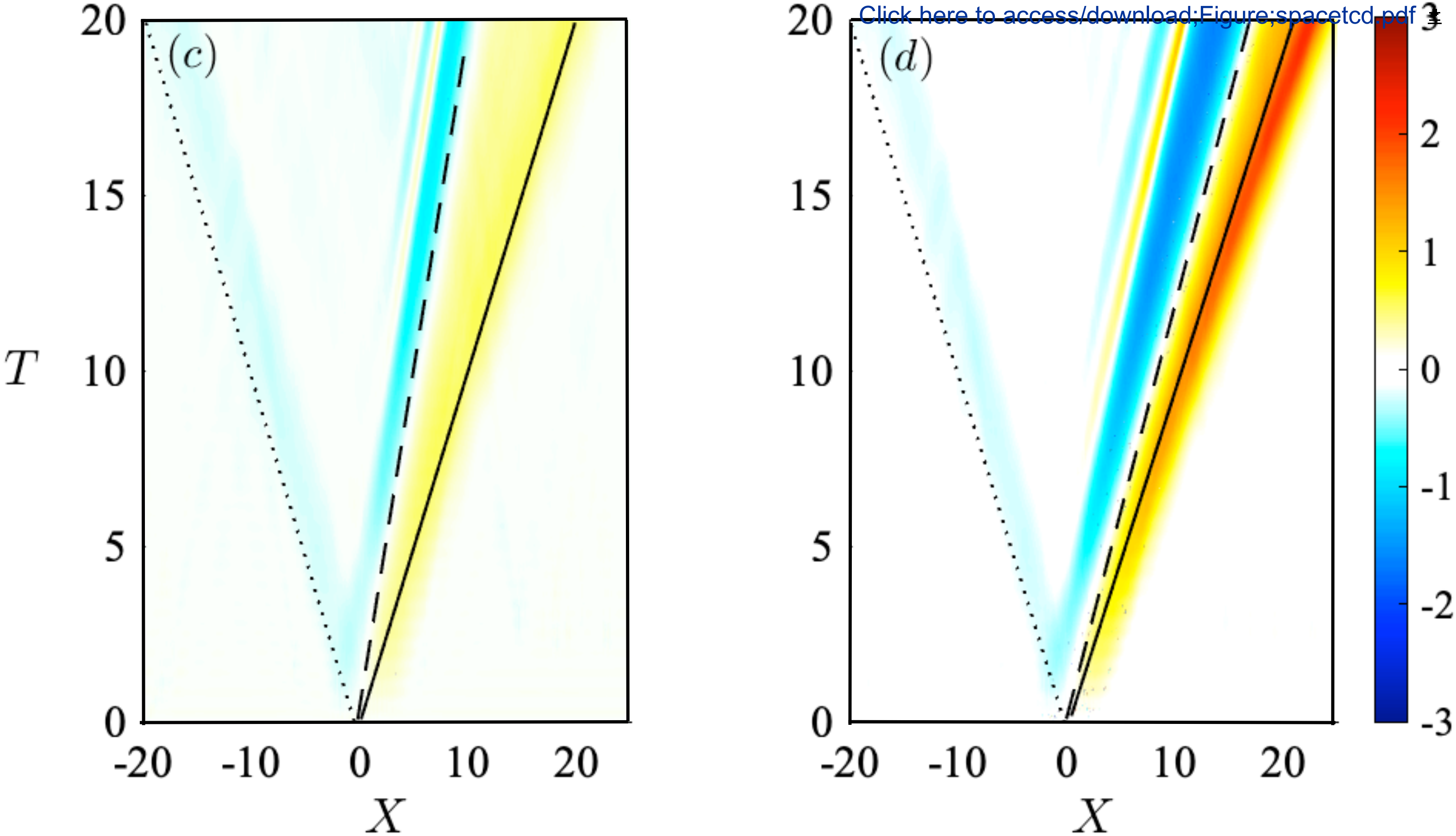

Click here to access/download;Figure;spacetime0.pdf

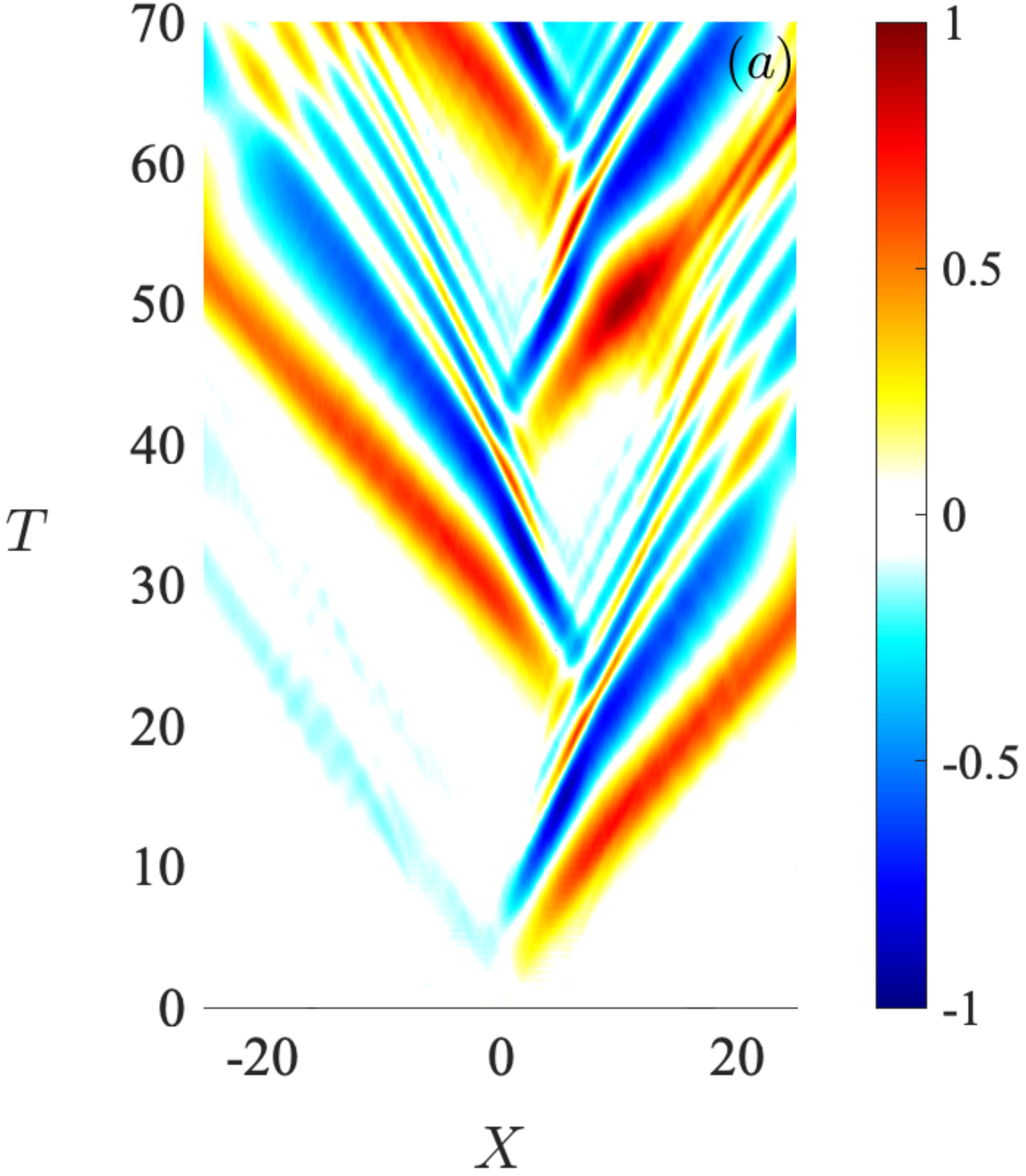

Click here to access/download;Figure;spacetime1.pdf

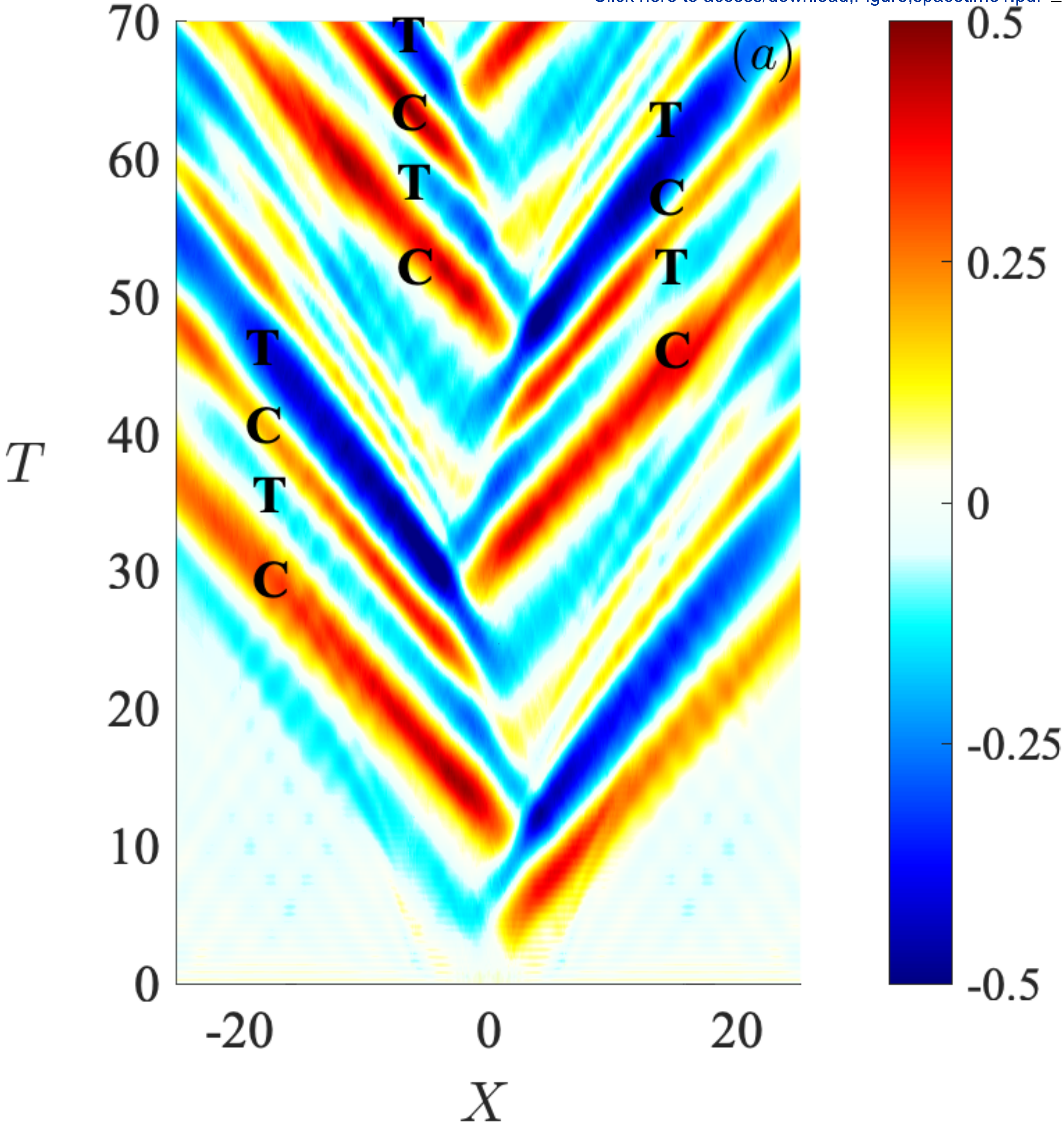

Click here to access/download;Figure;spec0.pdf

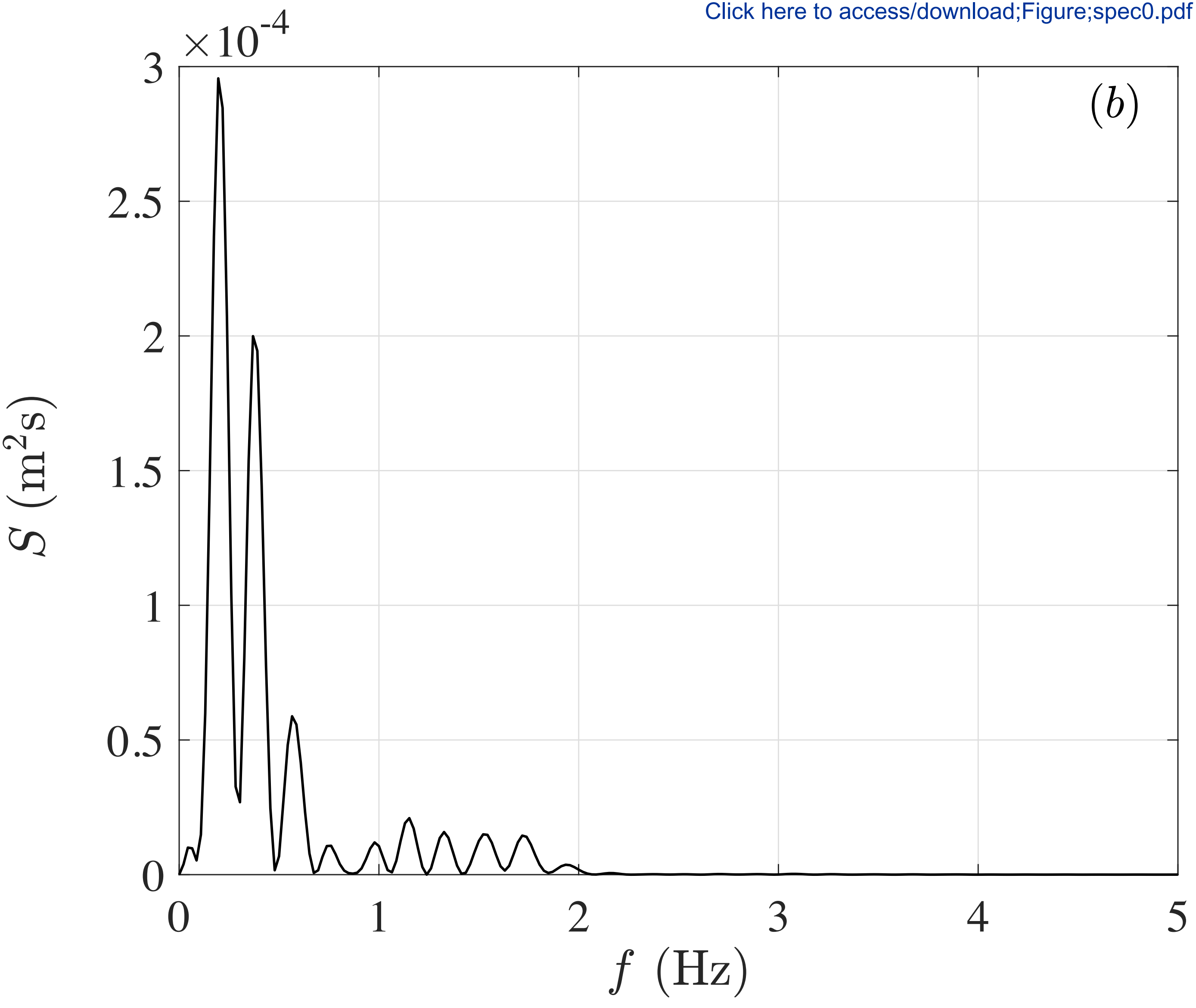

Click here to access/download;Figure;spec1.pdf

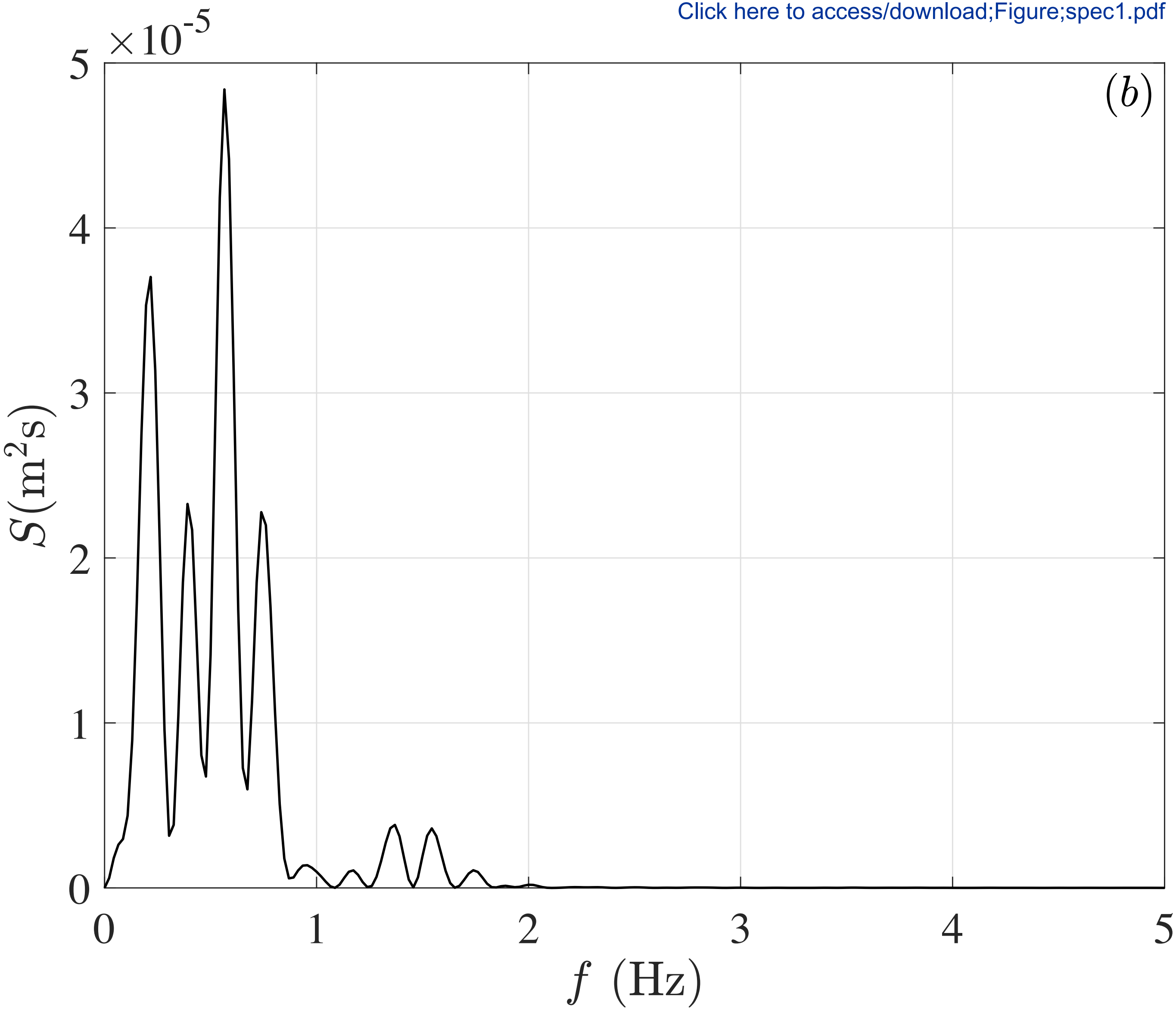

Click here to access/download;Figure;velplot.pdf

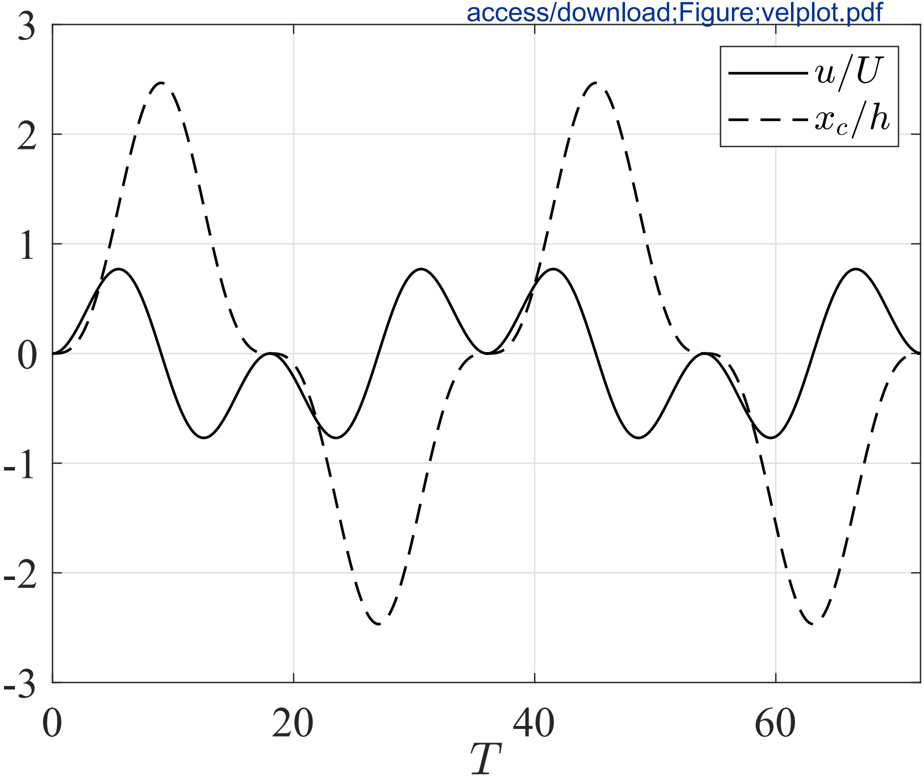

Click here to access/download;Figure;vort.pdf

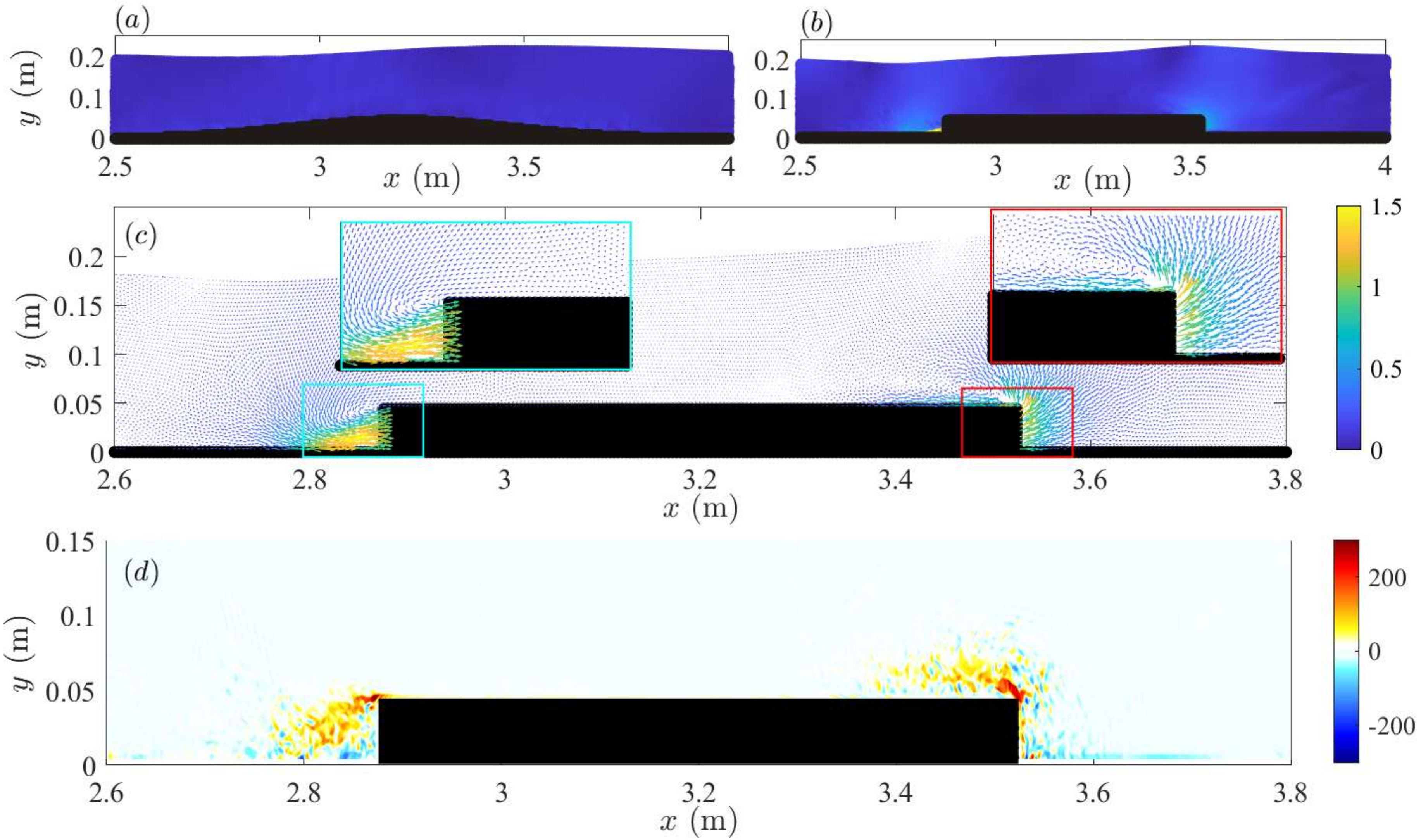

Declaration of interests

☒The authors declare that they have no known competing financial interests or personal relationships that could have appeared to influence the work reported in this paper.

☐The authors declare the following financial interests/personal relationships which may be considered as potential competing interests: